

UCD SCHOOL OF PHYSICS

---

# Current Retrieval from Remote Sensing Images of Ocean Waves

---

**Author:** Joseph Anderson

**Student ID:** 20493252

**Supervisors:** Susanne Støle-Hentschel & Frederic Dias

Friday 26<sup>th</sup> April, 2024



This thesis is submitted to University College Dublin in partial fulfilment of the requirements for  
the degree of BSc in Theoretical Physics.

## **Abstract**

This work analyses the factors that influence current retrieval for both simulated and physical waves using radar images. The Doppler shift velocities are related to the dispersion relation. These are found using one of three methods: least squares method, normalized scalar product method or polar current shell method for simulated data. The normalized scalar product method is found to give the best results. The depth dependent current is found using one of the following inversion methods: the effective depth method (EDM) or the newly introduced polynomial effective depth method (PEDM). For validation, the physical wave results are compared to measurements from an Acoustic Doppler Current Profiler (ADCP). This thesis has been the first study of the PEDM on real ocean wave radar images. We found that the PEDM performed better than the EDM in all cases. The PEDM provided an estimate of the current in shallower depths than the ADCP. We have also uncovered a limitation of the PEDM in cases involving high shear currents.

**Keywords:** Ocean Current, Radar Imaging, Spectral Analysis, Dispersion Relation.

## **Acknowledgments**

I would firstly like to express my gratitude to my supervisors, Professor Frederic Dias and Dr. Susanne Støle-Hentschel. They have both given me continued guidance and knowledge throughout the year which has allowed me to delve deeply into my research topic.

I would like to thank Benjamin Smeltzer who took time to meet with me during the year. This ensured that the project explored topics that would be of interest to academics within the field. I also appreciate the contributions of Rotem Soffer who provided the physical radar sequences.

This project has allowed me to improve my research and technical skills which would not have been possible without the support and resources from the UCD School of Physics. I am grateful for the support of my friends and family who have encouraged me during the academic year.

## **Declaration of Authorship**

I declare that all material in this thesis is my own work, except where there is clear acknowledgement and appropriate reference to the work of others.

# Contents

<b>1</b>	<b>Introduction</b>	<b>1</b>
1.1	Motivation . . . . .	1
1.2	Objectives . . . . .	1
<b>2</b>	<b>Theory</b>	<b>2</b>
2.1	Dispersion Relation . . . . .	2
2.2	Dispersion Relation using Wave Spectrum . . . . .	3
2.3	Doppler Current and Depth-Dependent Current Relationship . . . . .	4
2.3.1	Linear Inviscid Equation of Motion . . . . .	4
2.3.2	Boundary Conditions . . . . .	5
2.3.3	Solution of Linear Inviscid Equation of Motion . . . . .	6
<b>3</b>	<b>Methodology on Simulated Data</b>	<b>8</b>
3.1	Doppler Shift Measurement . . . . .	8
3.1.1	Least Squares Method . . . . .	8
3.1.2	Normalised Scalar Product Method . . . . .	10
3.1.3	Polar Current Shell Method . . . . .	12
3.2	Current Inversion . . . . .	14
3.2.1	Effective Depth Method . . . . .	14
3.2.2	Polynomial Effective Depth Method . . . . .	15
3.2.3	Simulated Waves . . . . .	16
<b>4</b>	<b>Field Data Measurements</b>	<b>19</b>
4.1	Radar Images . . . . .	19
4.2	ADCP Data . . . . .	20
4.3	Doppler Shift Measurement . . . . .	21
4.3.1	Anti-Aliasing . . . . .	21
4.3.2	Apply NSP and Fit Curves . . . . .	22
4.4	Current Inversion . . . . .	25

4.4.1	East Velocity Component . . . . .	27
4.4.2	North Velocity Component . . . . .	28
4.5	Limitations . . . . .	29
<b>5</b>	<b>Conclusion</b>	<b>30</b>

## List of Figures

1	The triplets (red circles) are the peaks in the ocean wave spectrum found through the 3D FFT. These triplets correspond to the linear dispersion relation (blue surface). This plot uses simulated data with parameters as outlined in Section 3 with the current profile $U(z) = e^{0.5z} + 0.05$ . . . . .	4
2	The resulting Doppler shifts $\tilde{c}(k)$ from the least squares method using an initial guess of $(U_x, U_y) = (0.2, 0.1)$ before fitting (left) and an initial guess of the true correct velocity (right). . . . .	9
3	The resulting Doppler shifts $\tilde{c}(k)$ separated into their $x$ and $y$ components from the NSP method on the simulated data with current direction $\psi = 0^\circ$ (left) and $\psi = 30^\circ$ (right). . . . .	11
4	The root mean square error of the Doppler shifts calculated from the NSP method with current direction $\psi = 0^\circ$ (left) and $\psi = 30^\circ$ (right). . . . .	11
5	The Doppler shifts $\tilde{c}(k)$ calculated using the standard PCS method with current direction $\psi = 0^\circ$ (left) and $\psi = 30^\circ$ (right). . . . .	13
6	The root mean square error of the Doppler shifts calculated from the PCS method with current direction $\psi = 0^\circ$ (left) and $\psi = 30^\circ$ (right). . . . .	13
7	The depth dependent current $U(z)$ with current direction $\psi = 0^\circ$ using the NSP Doppler shifts (left) and the PCS Doppler shifts (right). The EDM is plotted by points and the PEDM is plotted as a line for each current component. . . . .	17
8	The depth dependent current $U_y(z)$ component with current direction $\psi = 0^\circ$ using the NSP Doppler shifts (left) and the PCS Doppler shifts (right). The lower two wavenumbers are not included in the PEDM process. . . . .	17

9	The depth dependent current $U(z)$ with current direction $\psi = 30^\circ$ using the NSP Doppler shifts (left) and the PCS Doppler shifts (right). . . . .	18
10	Current component, $U_y(z)$ , with current direction $\psi = 30^\circ$ using the NSP (left) and the PCS (right) Doppler shifts. The lower three wavenumbers are not included in the PEDM fitting. . . . .	18
11	Illustrates the first $t = 0$ radar image of the sequence of images taken at 04:00, 19 <sup>th</sup> January 2022. The full radar image is shown (left) along with the rotated radar image (right). The extraction window in red is used to find the currents. . . . .	19
12	The ADCP averaged measurements are shown for the $U_{East}$ component (left) and for the $U_{North}$ component (right) for each of the radar sequences studied which were 18-23, 19-04 and 19-11. . . . .	20
13	The power spectrum is found along the $k_x = 0$ slice. It is clear the simulated data with $\psi = 0^\circ$ (left) has no aliasing present whereas the 19-04 field data has aliasing present (right). . . . .	21
14	The resulting anti-aliased spectrum along $k_x = 0$ for the 19-04 field data. . . . .	22
15	Shows the fitted curve to the filtered NSP points where the outliers have been detected based off their distance to the curve. Detected outliers are shown as blue points whereas non-outlier NSP points are shown as black points. . . . .	23
16	A polynomial is fitted to the ADCP data and $U_0$ which results in the depth dependent current $U(z)$ (left). This is used in the Stewart and Joy integral to give the estimate of the Doppler shift curve (right). . . . .	24
17	The fitted curves for both components of the Doppler shifts are plotted for the 18-23 (left) radar sequence, the 19-04 (right) radar sequence and the 19-11 (bottom) radar sequence. This method is applied to each component separately. . . . .	25
18	Current inversion methods are applied to the 18-23 radar sequence. Each method is plotted for the East component (left) and the North component (right). . . . .	26
19	Current inversion methods are applied to the 19-04 radar sequence. Each method is plotted for the East component (left) and the North component (right). . . . .	27

20	Current inversion methods are applied to the 19-11 radar sequence. Each method is plotted for the East component (left) and the North component (right). . . . .	27
21	The PEDM and EDM are compared for $U_{North}$ for each radar sequence. The difference with the ADCP measurements are plotted at depths where the EDM points are present. . . . .	29
22	The fitting of the current shell at a particular radius $k = 0.15$ (left). The PCS is performed for many different wavenumbers (right). . . . .	35

## List of Tables

1	RMSE values between the Doppler shift curves and the NSP Doppler shift points for each of the radar sequences. . . . .	24
2	Average residual values between the ADCP and each of the inversion methods for each radar sequence. . . . .	28

## List of Acronyms

**ADCP:** Acoustic Doppler Current Profiler

**FFT:** Fast Fourier Transform

**EDM:** Effective Depth Method

**PEDM:** Polynomial Effective Depth Method

**LS:** Least Squares

**ILS:** Iterative Least Squares

**NSP:** Normalised Scalar Product

**PCS:** Polar Current Shell

**RMSE:** Root Mean Squared Error

# 1 Introduction

## 1.1 Motivation

Current measurements are vital to how we understand the movement of oceans. The velocity and direction of the current can be important for a wide range of applications. Knowledge of the ocean current can contribute to more accurate weather forecasting [1]. Ocean currents are crucial to understanding the impact of an oil spill [2]. Ocean current measurement can lead to choosing more efficient shipping routes [3]. Tracking ocean currents can maximise energy generation from sea turbines [4]. There are also a multitude of other applications of current measurements.

Many different techniques have been used to measure ocean currents. Eulerian frameworks have been used which included instruments being attached to fixed moorings which either floated on the surface of the water or were submerged [5]. Lagrangian frameworks have been used involving drogues at different depths [6]. These in situ methods experience a broad range of challenges such as being expensive, time consuming to deploy, limited data collection area and other factors [7]. Recently, the most commonly used method is an Acoustic Doppler Current Profiler (ADCP) which measures the Doppler shift of sound reflected from the water at various distances in the water column. ADCP measurements of ocean currents have gained widespread acceptance and are commonly used in the field [8]. However, it is difficult to measure the current in the uppermost layer using ADCPs as the water particles are effected by both the currents and waves [9].

To avoid the deployment and retrieval of sensors, remote sensing can be a great alternative to in situ measurements. Currents can be mapped over a large area with a single radar image. This achieves the same degree of spatial coverage using in situ point sensors [10].

## 1.2 Objectives

This project will first focus on simulated waves. Existing methods will be used to extract the wavenumber-dependent Doppler shift velocity. The performance of these methods will be compared to the known Doppler shifts of the simulated waves. These Doppler shifts will be used in an inversion method to find the depth-dependent current. The factors that influence the accuracy of the current inversion method will be studied.

These methods will also be applied to ocean wave data from the Eastern Mediterranean Sea approximately 1.5 km off the coastline. This data was collected externally thanks to Rotem Soffer. Three specific radar sequences will be used. Effects from aliasing and noise will be reduced when finding the Doppler shifts. The inversion methods will be used to find the current profile which can be compared to data from an ADCP in the field. These radar sequences experience different levels of shear allowing us to compare the impact of shear on current inversion methods.

## 2 Theory

Estimating currents from wave measurements requires two distinct steps:

1. Measure the dispersion relation of the ocean waves and find the Doppler shift velocities as a function of wavenumber,  $\tilde{c}(k)$ . (Section 2.1 and Section 2.2)
2. Use the Doppler shift velocities to invert the current profile giving the measured current as a function of depth,  $U(z)$ . (Section 2.3)

### 2.1 Dispersion Relation

In this section, ocean waves are assumed to be linear water waves. The following assumptions are made: the fluid is incompressible and inviscid, the flow is irrotational and the wave amplitudes are small compared to the wavelength. We assume that the linearised water-wave problem has harmonic wave solutions. Thus, we can derive the dispersion relationship for water waves:

$$\omega_0(\vec{k}) = \sqrt{gk \tanh(kh)}. \quad (1)$$

This relates the wave angular frequency  $\omega_0$  and the modulus of the wavenumber  $k = |\vec{k}|$ . Here,  $g$  is the acceleration due to gravity,  $\vec{k} = (k_x, k_y)$  and  $h$  is the depth of the water which is assumed to be constant.

The addition of an ocean current beneath the surface of the ocean will change the dispersion relation. Assuming a constant current in all spatial dimensions, with variation due to depth neglected

it can be derived by extending Appendix A to 2D:

$$\omega_{DR}(\vec{k}) = \sqrt{gk \tanh(kh)} + \vec{k} \cdot \vec{U}, \quad (2)$$

where  $\vec{U}$  is the current velocity. It is important to note that the assumption that the current is constant at all depths is not a realistic one. Thus,  $\vec{U}$  does not actually represent the true velocity of the current. Instead, it represents a wavenumber dependent Doppler shift velocity  $\vec{c}(k)$ . This will be used to find the depth dependent current through the relationship in Section 2.3.

## 2.2 Dispersion Relation using Wave Spectrum

The dispersion surface  $\omega_{DR}(k_x, k_y)$  can be approximately found using the wave spectrum of the radar images. The free surface of the radar images is defined as  $I(x, y, t)$ , where  $x, y$  correspond to the horizontal spatial dimensions and  $t$  is time. The radar backscatter image can be transformed from the time-space domain to the wavenumber-frequency domain using a 3D Fast Fourier Transform (FFT). In the spectral model of the ocean, the water surface can be represented by a linear summation of sinusoidal waves:

$$I(\vec{x}, t) = \sum_{i=1}^N A_i \cos(\vec{k}_i \cdot \vec{x} - \omega_i t), \quad (3)$$

where  $\vec{k} = (k_x, k_y)$ ,  $\vec{x} = (x, y)$  and  $N$  represents the number of wave components used [11]. The 3D FFT finds the combination of sinusoidal waves that make up the ocean surface. It can then find the frequency dependence of these waves on specific wavenumbers. The resulting spectrum is a function of three variables:  $k_x$ ,  $k_y$ , and frequency  $\omega_{DR}$  [12]. From the dispersion relation in Equation (2) only certain combinations of  $(k_x, k_y, \omega_{DR})$  are allowed. The greatest signal of the spectrum from the 3D FFT corresponds to these triplets which satisfy the dispersion relation shown in Figure 1. The angular frequencies  $\omega_{DR}$  can be found at certain triplet values using the method outlined in Appendix B used in Shen *et al.* [13]. Looking at Equation (2) it is clear that now only the Doppler shift current,  $\vec{c}(k)$ , is left to find. This can be found using algorithms such as the least squares method, normalised scalar product method or the polar current shell method.

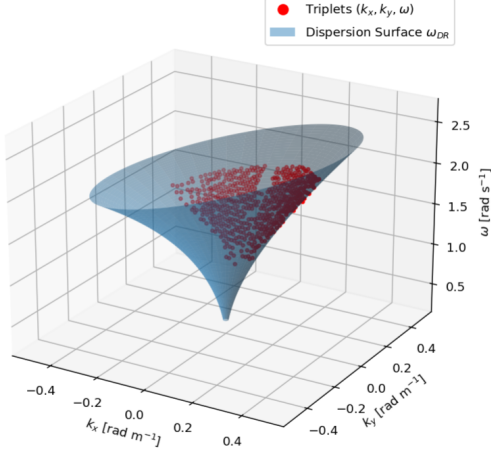


Figure 1: The triplets (red circles) are the peaks in the ocean wave spectrum found through the 3D FFT. These triplets correspond to the linear dispersion relation (blue surface). This plot uses simulated data with parameters as outlined in Section 3 with the current profile  $U(z) = e^{0.5z} + 0.05$ .

## 2.3 Doppler Current and Depth-Dependent Current Relationship

Ocean wave theory is used to find the relationship between the Doppler shifts and the depth-dependent current. It is derived using the perturbation approach shown by Stewart and Joy [14]. For Equation (2) it was assumed that the currents are uniform in depth. However, this is not the case as currents are influenced by waves and wind causing currents to be dependent on depth.

### 2.3.1 Linear Inviscid Equation of Motion

Consider the velocity field  $(u, w)$  in the Cartesian coordinates  $(x, z)$  where  $z$  is in the vertical direction and  $x$  is the direction waves travel. The linearised Euler equations in the  $x$  and the  $z$  directions are [15]:

$$\rho(u_t + \hat{U}u_x + \hat{U}'w) = -p_x, \quad (4)$$

$$\rho(w_t + \hat{U}w_x) = -p_z, \quad (5)$$

where  $\hat{U}$  is the mean velocity in the  $x$  direction and  $p$  is the dynamic pressure where we define  $\hat{U}'(z) = \frac{d\hat{U}(z)}{dz}$ . The continuity equation is:

$$u_x + w_z = 0. \quad (6)$$

Let's consider a streamfunction in the form:

$$\psi = f(z)e^{ik(x-ct)}. \quad (7)$$

Taking  $\frac{\partial}{\partial z}(4)$  and  $\frac{\partial}{\partial x}(5)$  the pressure term can be eliminated by the symmetry of second order partial derivatives. Then, substituting in that the streamfunction satisfies  $u = \frac{\partial \psi}{\partial z}$  and  $w = -\frac{\partial \psi}{\partial x}$  leads to the linear, inviscid equation where we define  $\hat{U}''(z) = \frac{d^2\hat{U}(z)}{dz^2}$  [15]:

$$f'' + \left( \frac{\hat{U}''}{c - \hat{U}} - k^2 \right) f = 0. \quad (8)$$

### 2.3.2 Boundary Conditions

Let the free surface of the water be  $\eta(x, t)$ . We define the linearised free surface to be  $z = 0$ , with the ocean floor being defined as  $z = -h$ . The dynamic boundary condition comes from neglecting quadratic terms in the unsteady Bernoulli equation [16]. At the free surface the condition is:

$$p(0) - \rho g \eta(x, t) = 0, \quad (9)$$

where  $\eta(x, t)$  is the displacement of the free surface from its mean position [15]. This can be used to rewrite Equation (4) to include the free surface condition as:

$$u_t + \hat{U} u_x + \hat{U}' w + g \frac{\partial \eta}{\partial x} = 0 \quad , \quad z = 0. \quad (10)$$

The kinematic boundary condition requires that the motion of the water surface is in agreement with the velocity components of the water particles [17]. The material derivative of the difference between the vertical coordinate of a water particle and the free surface results in the condition:

$$\frac{\partial \eta}{\partial t} + \hat{U} \frac{\partial \eta}{\partial x} = w \quad , \quad z = 0. \quad (11)$$

The dynamic boundary condition can be used with  $u_x$ ,  $u_t$  and  $w$  to find a general form for the free surface  $\eta$ . This can be substituted into the kinematic boundary condition to find the following

condition on  $f$  at the mean free surface  $z = 0$ :

$$\frac{df}{dz}(z = 0) = \left( \frac{\hat{U}'}{\hat{U} - c} + \frac{g}{(\hat{U} - c)^2} \right) f(z = 0). \quad (12)$$

### 2.3.3 Solution of Linear Inviscid Equation of Motion

An approximate solution of Equation (8) is sought. It is assumed that the surface current is small in comparison to the wave phase velocity i.e  $\hat{U}(z) = \epsilon c_1 U(z)$  where  $\epsilon \ll 1$ ,  $c_1$  is the dimensional wave velocity and  $U(z)$  is the non dimensional mean current velocity. The solution of Equation (12) is expanded in powers of  $\epsilon$  giving  $f = f_1 + \epsilon f_2 + \epsilon^2 f_3$  and  $c = c_1 + \epsilon c_2 + \epsilon^2 c_3$ . The first order is considered meaning that  $f = f_1$  and  $c = c_1$  which can be used in Equation (8) to give:

$$f_1'' - k^2 f_1 = 0. \quad (13)$$

The second order solution uses  $f = f_1 + \epsilon f_2$  and  $c = c_1 + \epsilon c_2$  which is used in Equation (8). Using that  $\epsilon \ll 1$  and that the coefficients of  $\epsilon$  are equivalent gives:

$$f_2'' - k^2 f_2 = U'' f_1. \quad (14)$$

The first and second order solutions can be put into the boundary condition from Equation (12) and evaluated at  $z = 0$ . Then, using similar approximations surrounding the fact that  $\epsilon \ll 1$  it can be shown that the boundary condition becomes:

$$f_1' - \frac{g}{c_1^2} f_1 = 0, \quad (15)$$

$$f_2' - \frac{g}{c_1^2} f_2 = \left( \frac{2g}{c_1^2(U - \frac{c_2}{c_1})} - U' \right) f_1. \quad (16)$$

The solution of Equation (13) is  $f_1 = ae^{kz}$  with  $k = \frac{g}{c_1^2}$ . This can be substituted into Equation (14) to give:

$$f_2'' - k^2 f_2 = U'' a e^{kz}. \quad (17)$$

The homogeneous version of Equation (17) has solution  $f_2(z) = Be^{kz} + De^{-kz}$ . Meanwhile, the particular solution can be found using the standard formula for the method of variation of parameters. Using integration by parts on the method of variation of parameters formula it can be found that the particular solution satisfies:

$$f_{2,p}(z) = -ae^{-kz} \int_{-\infty}^z U' e^{2kz} dz. \quad (18)$$

Thus, the general solution is:

$$f_2(z) = ae^{kz} - ae^{-kz} \int_{-\infty}^z U' e^{2kz} dz. \quad (19)$$

This general solution of  $f_2(z)$  can be used in Equation (16) along with using that  $c_1^2 = \frac{g}{k}$  and  $c = c_1 + \epsilon c_2$  which results in the phase velocity of the wave:

$$c_p = c_1 + 2k \int_{-\infty}^0 U(z) e^{2kz} dz. \quad (20)$$

Thus, given that  $c_p - c_1$  is the Doppler velocity we have derived that the Doppler shift can be approximated as a weighted average of the current profile as a function of depth:

$$\tilde{c}(k) = 2k \int_{-\infty}^0 U(z) e^{2kz} dz. \quad (21)$$

A similar approach can be extended resulting in the finite depth extension of Equation (21) above [18, 19]:

$$\tilde{c}(k) = \frac{2k}{\sinh(2kh)} \int_{-h}^0 U(z) \cosh[2k(h+z)] dz. \quad (22)$$

An inversion method is used to find the depth dependent current  $U(z)$  from the previously calculated  $\tilde{c}(k)$  using Equations (21) and (22). Algorithms such as the Effective Depth Method (EDM) or the Polynomial Effective Depth Method (PEDM) can be used to perform this task.

### 3 Methodology on Simulated Data

In this section each method will be introduced and then applied to simulated waves. The simulated wave fields are based on directional JONSWAP spectra in a water depth of 1000 m with a directional spreading of 30 implemented following Mitsuyasu *et al.* [20]. We study two wave fields which only differ in current direction of either 0° or 30°. The simulated wave fields occurred in a window of size 500 × 500 m over the course of 20 min. They had a range resolution of 7.5 m in both the  $x$  and  $y$  directions with a temporal resolution of 1 second. Further description of the sea state involving wave height, patch size and temporal parameters can be found in Støle-Hentschel *et al.* [21].

#### 3.1 Doppler Shift Measurement

The Doppler shift measurements can be found through measuring the dispersion relation using the wave spectrum to find  $\omega_{DR}$  and then using an algorithm to solve Equation (2). There are many algorithms that have been developed to do this such as the least-squares (LS) fitting technique [22], the weighted LS method [23], the iterative LS method (ILS) [24], the normalised scalar product (NSP) method [25] and the polar current shell method (PCS) [26]. In our study we will concentrate on the LS, NSP and PCS methods as these are commonly used in the field and have been tested extensively.

##### 3.1.1 Least Squares Method

This method involves a LS technique using the fundamental mode wave dispersion relationship. Velocity components are obtained through minimising the error in Equation (2). The error parameter is defined as:

$$Q = \sum_{i=1}^{N_1} [\omega_i - \omega_0(k_{xi}, k_{yi}) - k_{xi}U_x - k_{yi}U_y]^2, \quad (23)$$

where  $(k_{xi}, k_{yi}, \omega_i)$  are the wavenumber-frequency triplets,  $(U_x, U_y)$  are the respective current components,  $\omega_0(k_{xi}, k_{yi})$  is the wave frequency calculated by Equation (1) and  $N_1$  is defined as the number of triplets whose energy is higher than  $C_1$  of the spectral peak. In practice, a value of  $C_1 = 0.2$  is a common choice [27].

Simulated wave fields were studied to attempt to verify the LS algorithm. The wavenumber-

frequency triplets were found using the method outlined in Section 2.2, resulting in 2154 triplets. The LS method was applied which resulted in some triplets being discounted due to their low energy values using the threshold value  $C_1 = 0.2$  as before. This threshold value aimed to reduce other signatures in the spectrum such as harmonics, aliasing and noise whilst also keeping enough data points to obtain a reasonable fit. There were 240 triplets that met this threshold criteria. However, naturally the minimisation required initial guesses of the velocity components.

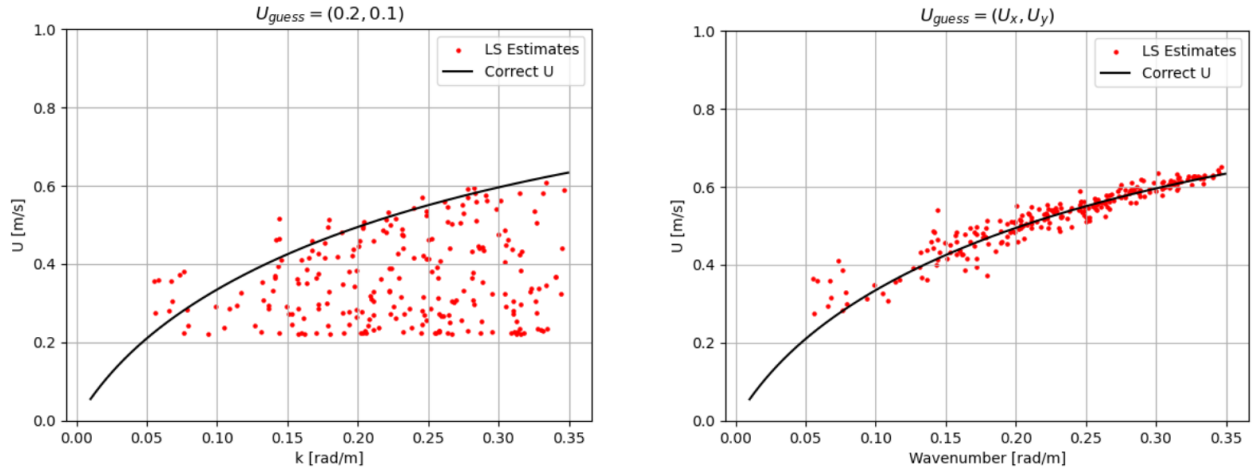


Figure 2: The resulting Doppler shifts  $\tilde{c}(k)$  from the least squares method using an initial guess of  $(U_x, U_y) = (0.2, 0.1)$  before fitting (left) and an initial guess of the true correct velocity (right).

It is evident from Figure 2 that the output of the least squares method is heavily reliant on the initial guess given to the LS method. Even with the exact correct initial values, there is still noise produced in the Doppler measurements. This is commonly a result of an improper choice of the threshold value [27]. Variation of this threshold value did not result in any improvement in the Doppler shifts. The threshold procedure causes noise to play a relevant role particularly at lower levels of the measured spectrum which was one motivation for developing the NSP method [25]. The LS method has been improved to the ILS and other such variations, however, these were not studied due to their poor relative performance in high current sea states [28]. In such states, aliasing has an increased effect on the calculation of the Doppler shifts and so the NSP or the PCS method are commonly preferred [12].

### 3.1.2 Normalised Scalar Product Method

The NSP method can also be utilised to find the Doppler shifts. We consider the wavenumber bins with center values  $k_i$  and half width  $\delta k$ . For each center wavenumber value we can define a masked spectrum  $F_i$  where energy outside the wavenumber bin is set to zero:

$$F_i(\vec{k}, \omega) = \begin{cases} \sqrt{P(\vec{k}, \omega)}, & \text{if } |k - k_i| \leq \delta k \\ 0, & \text{otherwise} \end{cases} \quad (24)$$

Due to the symmetries of the Fourier transform of a signal comprised of real numbers, the characteristic function  $G$  is defined as:

$$G(\vec{k}, \omega, \tilde{c}) = \exp\left(-2\left[\frac{(\omega - \omega_{\text{DR}}(\vec{k}, \tilde{c}))}{a}\right]^2\right) + \exp\left(-2\left[\frac{(\omega + \omega_{\text{DR}}(\vec{k}, \tilde{c}))}{a}\right]^2\right), \quad (25)$$

where  $a$  is a parameter that controls the spectral width in frequency of the dispersion relation shell [21]. The normalised scalar product as a function of the unknown current components  $(U_x, U_y)$  is defined as:

$$V(U_x, U_y) = \frac{\langle |F_i(\vec{k}, \omega)|, G(\vec{k}, \omega, U_x, U_y) \rangle}{\sqrt{P_F \cdot P_G}}, \quad (26)$$

where  $P_F$  and  $P_G$  are the powers associated to the image of the spectrum  $F_i$  and  $G$  respectively. The value of  $V$  is maximised with respect to the Doppler shift components. This implies the greatest overlap between the dispersion relation shell defined by the characteristic function and that of the true spectrum. Importantly, the NSP method does not require choosing an optimal threshold for the image spectra [29].

The NSP method is applied to both simulated wave fields. To reduce the computational cost of the NSP method the search range of the current velocities is  $[-1, 1]$  m/s as the current is not high in this simulated wave field. A resolution of 0.1 m/s is initially used to find  $(U_{x_0}, U_{y_0})$ . This is followed by another search range of size  $\pm 0.1$  m/s around  $(U_{x_0}, U_{y_0})$  with a resolution of 0.01 m/s. Two simulated wave fields are studied where only the current directions differ. The current directions of each simulated wave field are  $\psi = 0^\circ$  and  $\psi = 30^\circ$  respectively.

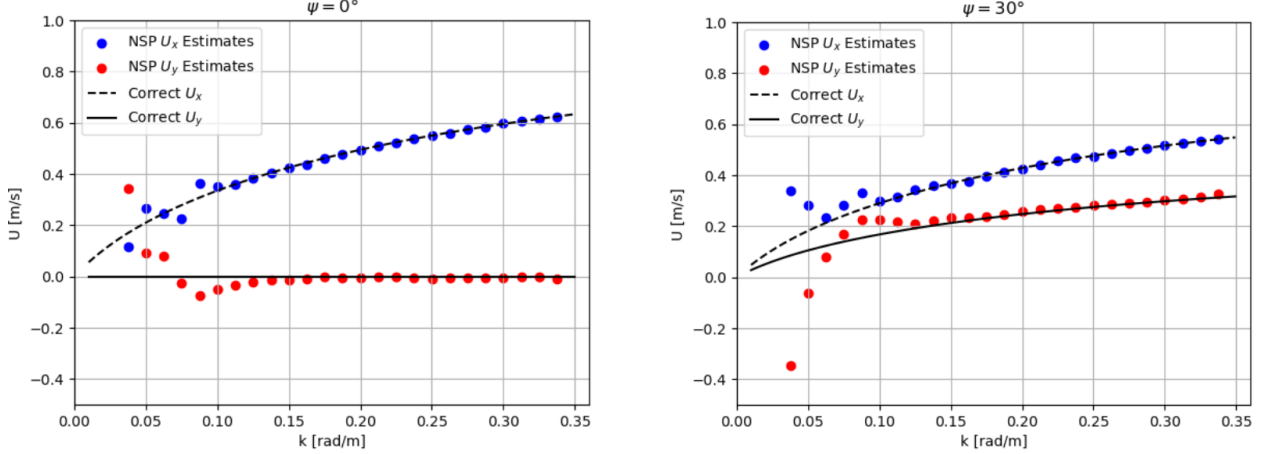


Figure 3: The resulting Doppler shifts  $\tilde{c}(k)$  separated into their  $x$  and  $y$  components from the NSP method on the simulated data with current direction  $\psi = 0^\circ$  (left) and  $\psi = 30^\circ$  (right).

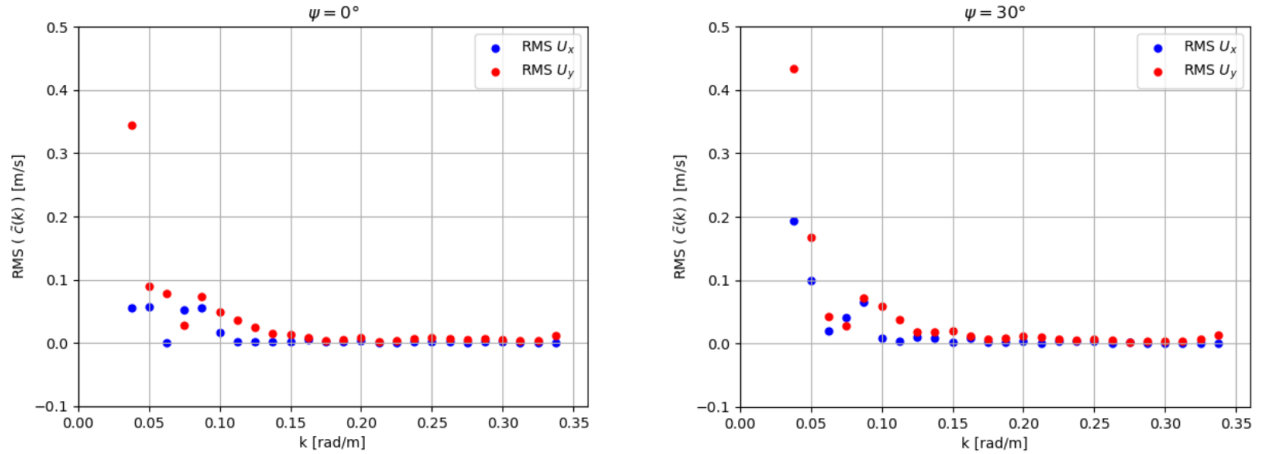


Figure 4: The root mean square error of the Doppler shifts calculated from the NSP method with current direction  $\psi = 0^\circ$  (left) and  $\psi = 30^\circ$  (right).

The NSP method provides much improved Doppler shift estimates. Similar to previous studies the root mean squared error of the Doppler shifts is highest for low wavenumbers and decreases towards zero for higher wavenumbers [21]. This can be attributed to spectral leakage which strongly affects low wavenumbers [30].

Spectral leakage is caused by the relationship between the window size and the observed wavelength. The spectral estimate improves, when there are more ocean wave wavelengths included in the window. Spectral leakage is a result of the waves not matching the windows. This leads to the

wave not being represented by a single wave component which means that other wave components need to compensate for this. This occurs in greater intensity for lower wavenumbers. Tapering and zero-padding the data can improve effects of spectral leakage however effects from spectral leakage will never be completely mitigated.

### 3.1.3 Polar Current Shell Method

Recently, the PCS algorithm has been developed which involves a sinusoidal curve-fitting process in polar coordinates. This method requires two main steps after finding the dispersion triplets as in Section 2.2:

1. *Transformation to the PCS:* The coarse dispersion shell,  $\omega_0(k_x, k_y)$  is  $\omega_i$  for the triplet pairs and zero elsewhere. The current-induced dispersion relation in Equation (2) can be rewritten using the definition of the dot product of Euclidean vectors:

$$\omega_U(k_x, k_y) = \vec{k} \cdot \vec{U} = kU \cos \bar{\theta} = \omega_0(k_x, k_y) - \sqrt{gk}, \quad (27)$$

where  $\bar{\theta}$  represents the intersection angle between the current direction and the wave vector and  $\omega_U(k_x, k_y) = \vec{k} \cdot \vec{U}$  represents the frequency shift by the current (current shell). The term  $\sqrt{gk}$  is the deep water limit of the dispersion relation. The Cartesian current shell  $\omega_U(k_x, k_y)$  can be transformed into the polar current shell  $\omega_U(k, \theta_{\vec{k}})$ .

2. *Current Parameters:* Noise can still occur in the polar current shell. This noise can severely effect the least squares fitting and thus, must be removed. This can be performed using a Grubbs' test as for a particular radial direction in the wavenumber plane the intersection angle  $\bar{\theta}$  is fixed [31]. Outliers and points in which  $\omega_0(k_x, k_y) = 0$  are removed from the fitting process. A least squares curve fitting is performed in each radial direction using the model function:

$$f(U, \bar{\theta}) = \frac{\omega_U}{k} = U \cos \bar{\theta}. \quad (28)$$

To maintain a good fit it is required that there must be a minimum ten points being fitted [29]. The process is aborted for the radius if the number of points is below this value. The angle

corresponding to the maximum of the estimated function is the current direction with the amplitude of the sinusoid being the current speed.

The PCS method is applied to the two simulated wave fields where only the current directions differ. Again, the current directions of each simulated wave field are  $\psi = 0^\circ$  and  $\psi = 30^\circ$  respectively. The PCS method was repeated for a collection of wavenumbers between 0 rad/m and 0.35 rad/m with an increment of 0.01 rad/m.

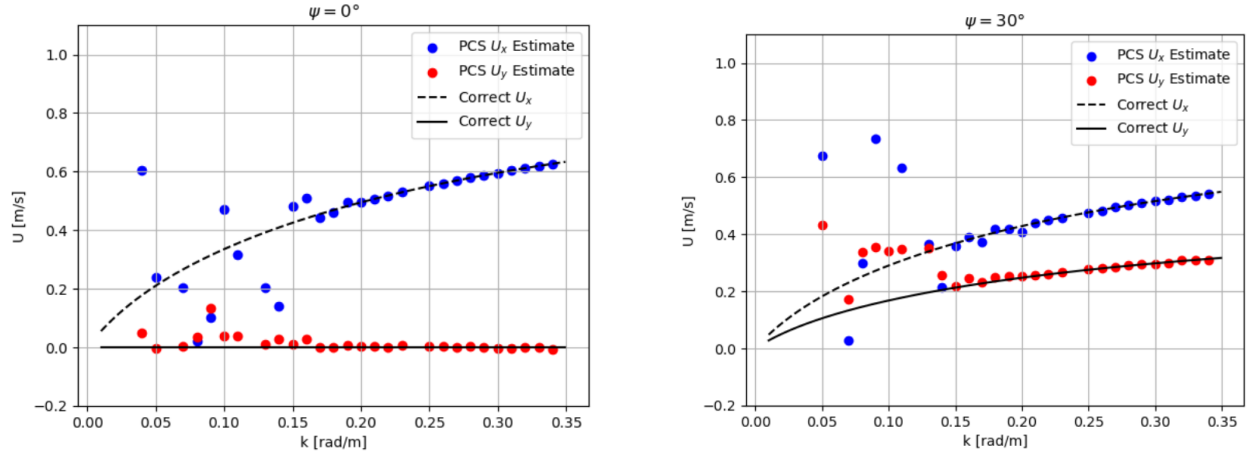


Figure 5: The Doppler shifts  $\tilde{c}(k)$  calculated using the standard PCS method with current direction  $\psi = 0^\circ$  (left) and  $\psi = 30^\circ$  (right).

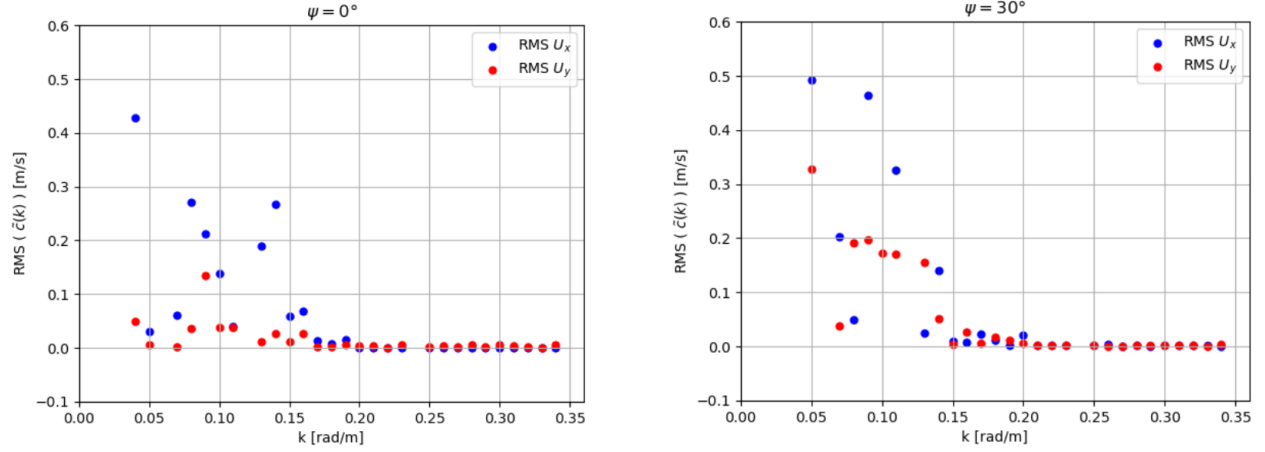


Figure 6: The root mean square error of the Doppler shifts calculated from the PCS method with current direction  $\psi = 0^\circ$  (left) and  $\psi = 30^\circ$  (right).

From Figures 5 and 6, it is clear that the PCS method fits well for higher wavenumbers with a

similar accuracy to that of the NSP method which was expected [29]. However, for low wavenumbers the PCS method has a larger error than the NSP had. More low wavenumber Doppler shifts have errors in them in the PCS case than the NSP case. As discussed for the NSP, spectral leakage can often impact the measurement for low wavenumbers. It seems that the PCS method amplifies these effects. The wavenumber resolution could be attributed to this amplification. In the NSP method the wavenumber resolution is further refined due to the decrease in search range for velocities. In the PCS method the wavenumber resolution remains constant.

The PCS method is limited in its nature due to the dependence on a large amount of triplet points to be found to ensure accurate sinusoidal fitting. The number of triplet points is usually large for simulated data due to the associated low amount of noise on the wave spectrum measurement. However, when applying this method to real ocean wave data the number of triplets that meet the criteria outlined in Section 2.2 can drastically decrease.

## 3.2 Current Inversion

The Doppler shift velocity  $\tilde{c}(k)$  found in Section 3.1 represents a weighted average of the current as a function of depth, as approximated by Equation (21). An inversion method is required to find the depth dependent current,  $U(z)$ . Methods such as the EDM, Ha-Campana and PEDM have been developed to perform this inversion. The Ha-Campana was found to demonstrate comparable accuracy to the EDM when comparing to ADCP measurements [12, 32]. However, the EDM's simplicity is preferred meaning that the Ha-Campana method will not be studied further in this text.

### 3.2.1 Effective Depth Method

This method assumes that the current profile has a specific functional form. First, we can assume that the current strength varies linearly with depth resulting in a profile of  $\vec{U}(z) = \vec{U}'z + \vec{U}_0$ , where  $\vec{U}_0$  is the surface current and  $\vec{U}'$  is the shear strength. Using this profile in Equation (21) and solving the integral we find:

$$\tilde{c}(k) = -\frac{\vec{U}'}{2k} + \vec{U}_0 = \vec{U} \left( z = -\frac{1}{2k} \right). \quad (29)$$

Hence, the Doppler shifts are equal to the current profile at a depth which we call the effective depth. For the linear profile assumption it is clear that the effective depth is  $z_{eff} = -(2k)^{-1}$ .

Assuming a logarithmic profile which is  $\vec{U}(z) = \vec{U}_0 - \frac{\vec{u}^*}{\kappa} \log(\frac{z}{z_0})$ , where  $\vec{u}^*$  is the friction velocity,  $\kappa$  is the Von Kármán constant and  $z_0$  is the roughness length. Similarly, this profile can be used in Equation (21) to find:

$$\tilde{c}(k) \approx \vec{U}_0 - \frac{\vec{u}^*}{\kappa} \log\left(\frac{1}{2krz_0}\right) = \vec{U}\left(z = -\frac{1}{3.56k}\right), \quad (30)$$

where  $r$  is 1.78. Hence, for the logarithmic profile assumption it is clear that  $z_{eff} = -(3.56k)^{-1}$ .

The EDM has been used extensively to find estimates of the current profile [33, 34]. It is commonly used due to its simple implementation. However, it requires a prior assumption to the functional form of the depth profile. In realistic cases it is rare that the current profile would resemble a linear or logarithmic profile.

### 3.2.2 Polynomial Effective Depth Method

The PEDM was proposed to prevent a prior assumption of the functional form of the depth profile [35]. The method begins with the standard EDM and fits the profile to a polynomial form and then scales the coefficients to give an improved estimate of the true current profile. Some polynomial is assumed to form the current profile which is given as  $U(z) = \sum_{n=0}^{\infty} u_n z^n$ . The resulting Doppler shifts can be found using the Stewart and Joy integral from Equation (21) yielding:

$$\tilde{c}(k) = \sum_{n=0}^{\infty} n! u_n \left(-\frac{1}{2k}\right)^n. \quad (31)$$

The  $(-2k)^{-1}$  is equal to the  $z_{eff}$  in the linear EDM. The PEDM explicitly follows using three key steps as outlined in Smeltzer *et al.* [35]:

1. Assign effective depths  $z_i = -(2k_i)^{-1}$  to each measured value of the Doppler shifts  $\tilde{c}_i$  using the EDM procedure.

2. Find  $U_{EDM}(z)$  through fitting the points  $(z_i, \tilde{c}_i)$  to a polynomial of degree  $n_{max}$ :

$$U_{EDM}(z) \approx \sum_{n=0}^{n_{max}} u_{EDM,n} z^n. \quad (32)$$

3. This can be scaled by a factor of  $n!$  to give the improved PEDM estimate to be:

$$U_{PEDM}(z) = \sum_{n=0}^{n_{max}} \frac{1}{n!} u_{EDM,n} z^n. \quad (33)$$

This method is in practice applied to both components of the velocity separately. The PEDM has been tested on laboratory measurements [35].

### 3.2.3 Simulated Waves

The EDM and PEDM are applied to the two simulated wave fields where only the current directions differ as before. It is assumed that the depth of the water is very large. The PEDM is performed down to a depth of 20 m as this allows us to see the discrepancy between the PEDM and the depth profile at greater depths. We will compare the inverted current from the PEDM using the NSP and PCS Doppler shifts against the true current profiles given to the simulated waves.

#### Data Set where $\psi = 0^\circ$

First, the  $\psi = 0^\circ$  case is studied. In Figure 7 we compare the difference in the PEDM when using the NSP method versus the PCS method. We can see that the PEDM represents  $U_x(z)$  quite well. For this component it is clear that using the NSP method means that the PEDM reconstructs the current profile much better than the PCS case. At greater depths the PEDM becomes less accurate for both input Doppler shifts. This is a result of the amplification of errors in the Doppler shifts due to the inversion process [12]. In particular, we saw that the Doppler shifts tended to be less accurate for the lower wavenumbers which correspond to the greater depths. We can recall from Section 3.1 that the PCS had an increased level of inaccuracy for the Doppler shifts at lower wavenumbers compared to the NSP method. Hence, we see the improved accuracy on the PEDM using the NSP method to find Doppler shifts over the PCS method. It is also important to note that the PEDM gives a closer fit to the actual profile in comparison to the EDM which is expected [35].

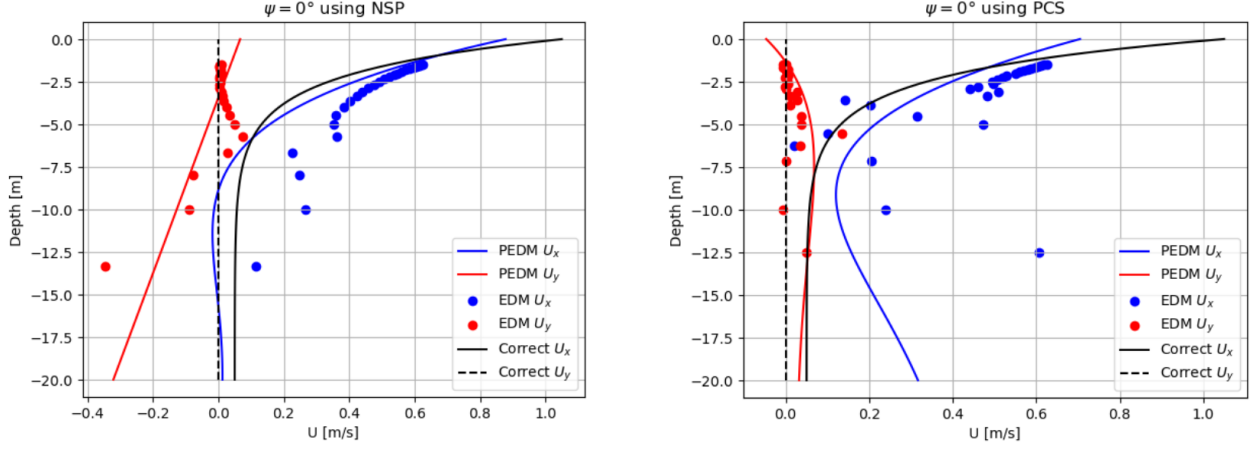


Figure 7: The depth dependent current  $U(z)$  with current direction  $\psi = 0^\circ$  using the NSP Doppler shifts (left) and the PCS Doppler shifts (right). The EDM is plotted by points and the PEDM is plotted as a line for each current component.

The  $U_y(z)$  component is not reconstructed well in either case in Figure 7 because this component is particularly sensitive to the input wavenumbers due to  $U_y(z)$  being close to 0. Hence, we can try to improve the performance of the PEDM by neglecting the smallest two wavenumbers. This removes the two EDM points at the greatest depths in the fitting process of  $U_y(z)$  during the PEDM which is shown in Figure 8. Again, the improved performance of the PEDM when using the NSP Doppler shifts instead of the PCS Doppler shifts is evident.

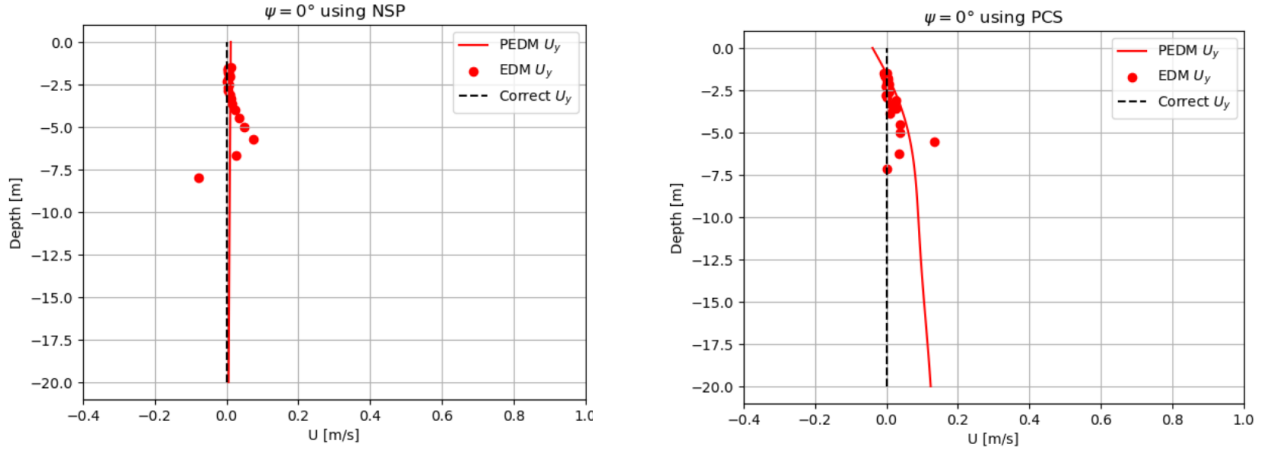


Figure 8: The depth dependent current  $U_y(z)$  component with current direction  $\psi = 0^\circ$  using the NSP Doppler shifts (left) and the PCS Doppler shifts (right). The lower two wavenumbers are not included in the PEDM process.

### Data Set where $\psi = 30^\circ$

Figure 9 depicts the  $\psi = 30^\circ$  case. The  $U_x(z)$  component has a better PEDM fit for the NSP case than the PCS case again. The large variety in effective depth points leads to poor PEDM fitting.

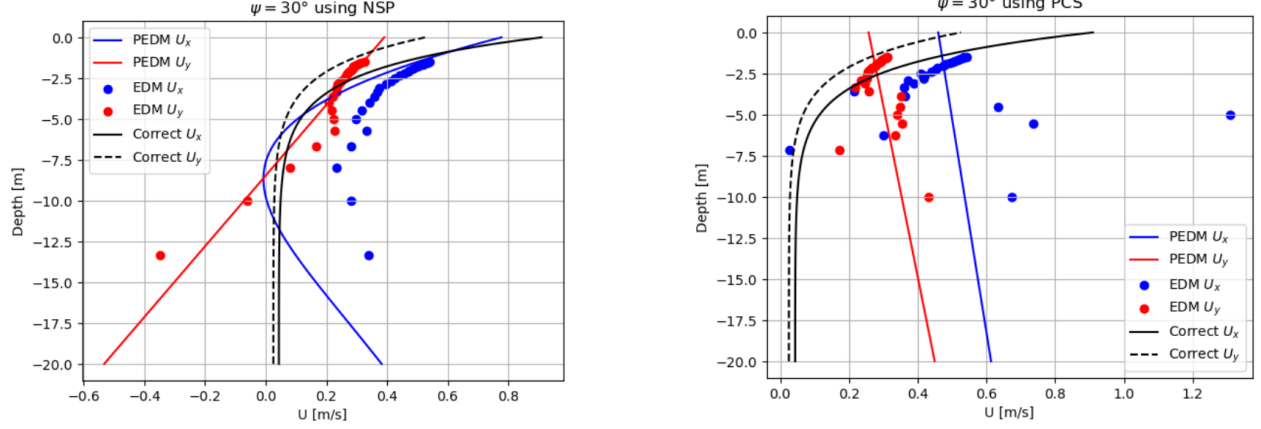


Figure 9: The depth dependent current  $U(z)$  with current direction  $\psi = 30^\circ$  using the NSP Doppler shifts (left) and the PCS Doppler shifts (right).

The  $U_y(z)$  component is plotted in Figure 10 with the lowest three wavenumbers in the Doppler shifts being neglected in the PEDM. The lowest three points were chosen based off visual inspection of the EDM points in Figure 9. These points were not similar to the behaviour of the correct current profile. The PEDM performs best for the case where the NSP Doppler shifts are used. They also have an improvement over the EDM points.

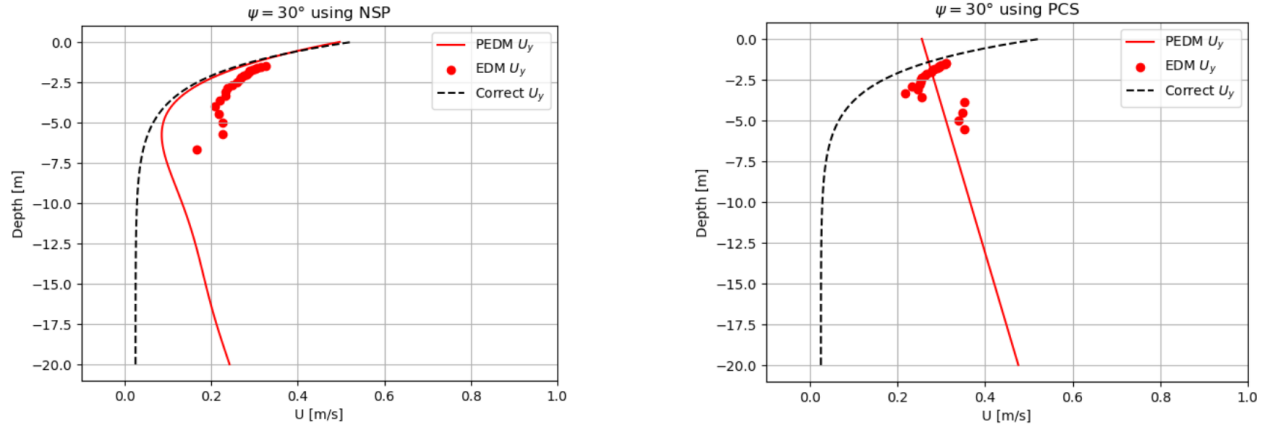


Figure 10: Current component,  $U_y(z)$ , with current direction  $\psi = 30^\circ$  using the NSP (left) and the PCS (right) Doppler shifts. The lower three wavenumbers are not included in the PEDM fitting.

## 4 Field Data Measurements

### 4.1 Radar Images

An X-band marine radar was located at ( $32^{\circ} 07' 50.0''N$ ,  $34^{\circ} 47' 14.0''E$ ) near HaTsuk beach. It captured radar images of a circular region with a radius of approximately 4 km with the radar at its centre. This area includes a section of ocean and a section of land. The radar operated with a rotation period of 2.46 seconds with a range resolution of 3.75 m. For a good frequency resolution, radar sequences of 15 min were analysed [21]. The radar sequence contained 366 images. Radar sequences of 15 min were extracted at every hour. We studied a period of a storm with high wind speeds and high significant wave heights starting at 21:00, 18<sup>th</sup> January 2022 until 18:00, 20<sup>th</sup> January 2022.. In such conditions, it is assumed that a strong shear can develop. Due to time constraint we concentrated on 3 particular hours.

The ADCP was located approximately 1.5 km off the coast at ( $32^{\circ} 08' 04.8''N$ ,  $34^{\circ} 46' 27.7''E$ ). We took a  $500 \times 500$  m extraction window with the ADCP located at the centre so that we could compare the ADCP measurements to the radar measurements. The radar image was then rotated clockwise by  $80^{\circ}$  so that the extracted window was in the main wave direction.

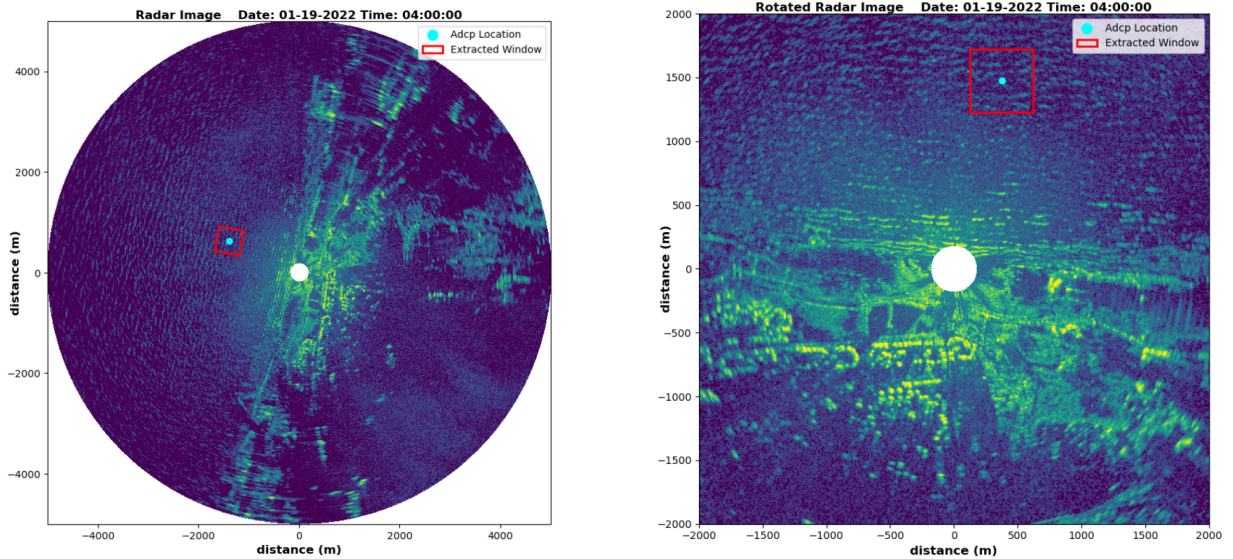


Figure 11: Illustrates the first  $t = 0$  radar image of the sequence of images taken at 04:00, 19<sup>th</sup> January 2022. The full radar image is shown (left) along with the rotated radar image (right). The extraction window in red is used to find the currents.

## 4.2 ADCP Data

The ADCP being used in the field was a Nortek Signature 1000 which was mounted on the sea bed. It employed an acoustic surface tracking beam for the sea elevation and it also has four slanted beams for radial velocities, providing the horizontal velocities. The ADCP data is averaged over the 15 min time frame to smoothen any large fluctuations in current at specific times. The ADCP does not accurately measure the upper layers of the water column as the water particles are effected by the current and the waves [9]. This causes inaccuracies in the ADCP in upper layers. Hence, the ADCP measurements are cut off close to the surface usually at approximately the mean wave height for that particular 15 min.

For the purpose of this research we will look at the following hours of the data taken in January 2022: 23:00 on the 18<sup>th</sup>, 04:00 on the 19<sup>th</sup> and 11:00 on the 19<sup>th</sup>. In this text we will refer to these radar sequences as 18-23, 19-04 and 19-11 respectively. This selection was made based on the varying levels of shear seen at these times which is evident in Figure 12. Both components at these times experience different levels of shear. Shear is defined as the sharp increase in velocity with a small increase in depth. The  $U_{East}$  component has high shear for each radar sequence. The  $U_{North}$  component has significantly less shear. These data sets can be used to test the performance of the PEDM and the EDM in varying levels of shear.

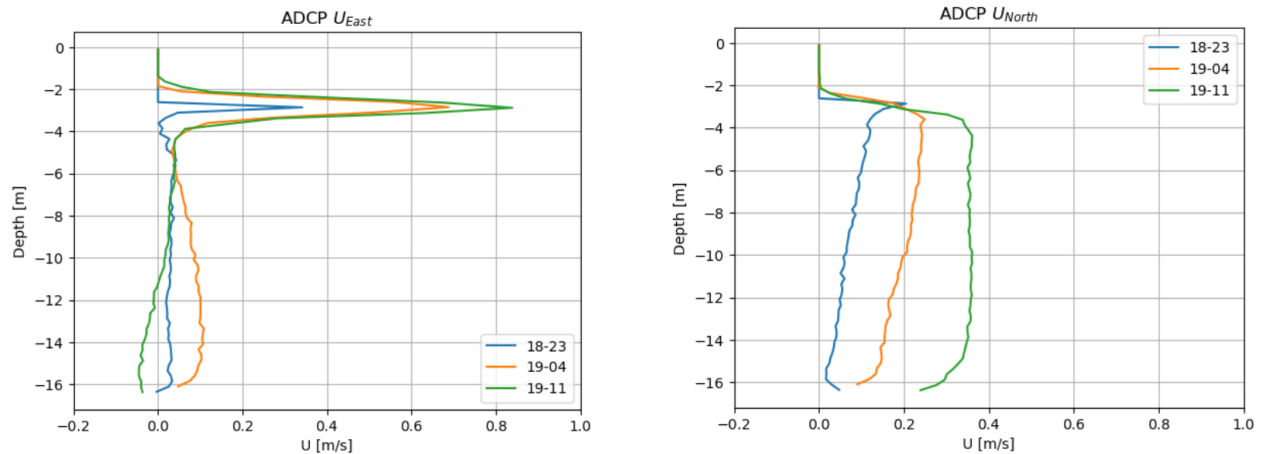


Figure 12: The ADCP averaged measurements are shown for the  $U_{East}$  component (left) and for the  $U_{North}$  component (right) for each of the radar sequences studied which were 18-23, 19-04 and 19-11.

## 4.3 Doppler Shift Measurement

The PCS method was tested on the anti-aliased radar data. However, there were insufficient triplets that met the threshold criteria which resulted in poor fitting of the sinusoidal (shown in Appendix C). This resulted in inaccurate estimations of the Doppler shifts. The simulated data showed that accurate Doppler shift measurements for the lower wavenumbers were required for an improved current profile. For the simulated data the NSP method gave the smallest error in velocities for the lower wavenumbers. Hence, to get the most accurate Doppler shifts the NSP method will be used.

### 4.3.1 Anti-Aliasing

Aliasing is often caused by under-sampling in either time or space. In this data set we observe that the resolution in time is coarser than the resolution in space. In the temporal domain higher frequencies are noticed but are not registered with the correct wavenumbers due to the less coarse spatial domain. This appears as extra artifacts of energy located away from the linear dispersion relation [12]. In the simulated data this issue was not present in the spectrum. However, in the field data there was aliasing present for all data studied shown in Figure 13. There is a symmetry present as the FFT is usually squared meaning that the dispersion relation leads to  $\omega_-(\vec{k}) = -\omega_{DR}(-\vec{k})$ . Hence, we see the clear dispersion relation for both  $\omega > 0$  and  $\omega < 0$ . The aliasing occurs for higher wavenumbers where the dispersion relation appears shifted.

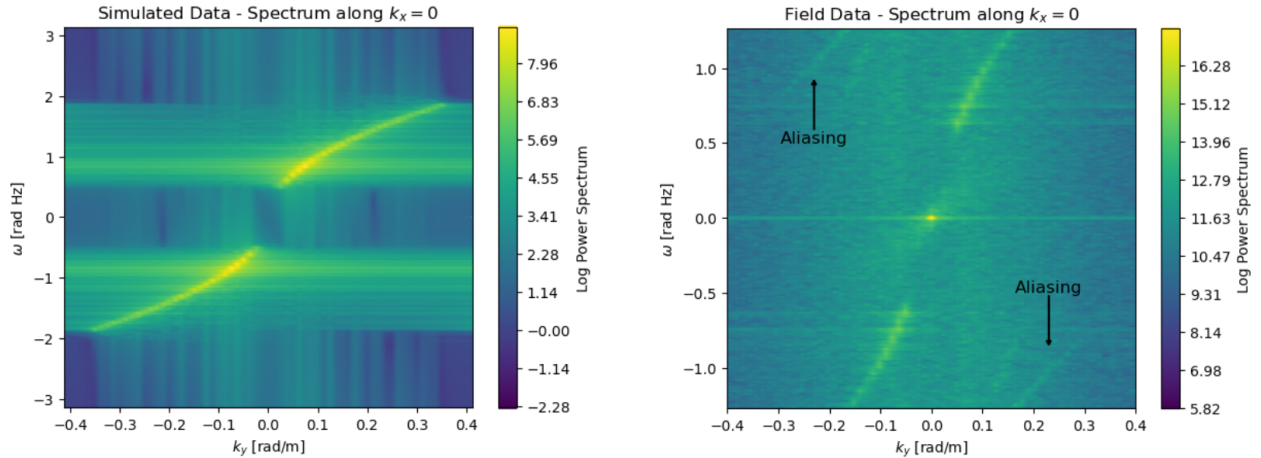


Figure 13: The power spectrum is found along the  $k_x = 0$  slice. It is clear the simulated data with  $\psi = 0^\circ$  (left) has no aliasing present whereas the 19-04 field data has aliasing present (right).

The NSP method does not take into account aliasing meaning that the dispersion relation at higher wavenumbers is ignored. A three-dimensional anti-aliasing is performed on the spectrum which follows on from the one-dimensional case shown in Støle-Hentschel *et al.* [36]. The aliased part of the spectrum is joined to the main dispersion relation resulting in the new extended spectrum in Figure 14. This is performed using the spectrum in polar co-ordinates. The one-dimensional case is applied to each slice of the azimuthal angle resulting in new extended spectrum's. These can be converted back to Cartesian co-ordinates leading to the anti-aliased spectrum.

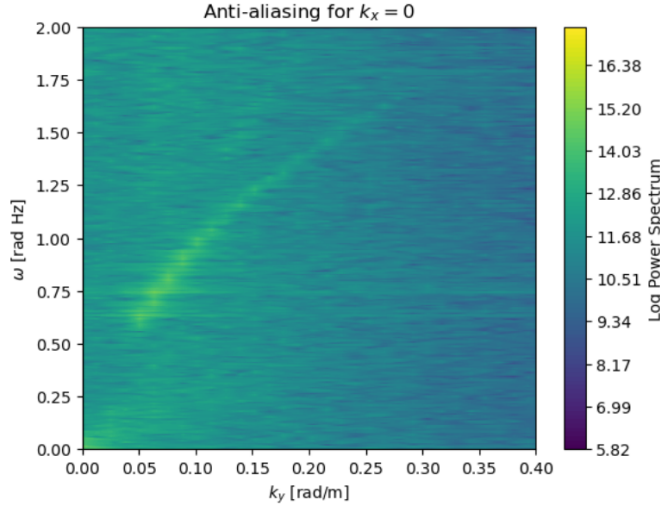


Figure 14: The resulting anti-aliased spectrum along  $k_x = 0$  for the 19-04 field data.

#### 4.3.2 Apply NSP and Fit Curves

The NSP method can be applied to this new extended spectrum. The velocities found by the NSP are for the rotated co-ordinates shown in Figure 11 on the right. The ADCP has been recorded in the set of co-ordinates pre-rotation corresponding to Figure 11 on the left. Hence, the resulting Doppler shift measurements from the NSP method need to be rotated by  $80^\circ$  anticlockwise using:

$$\begin{pmatrix} U_{East} \\ U_{North} \end{pmatrix} = \begin{pmatrix} \cos(\theta) & -\sin(\theta) \\ \sin(\theta) & \cos(\theta) \end{pmatrix} \begin{pmatrix} U_x \\ U_y \end{pmatrix}, \quad (34)$$

where  $\theta = 80^\circ$  is the rotation angle and  $U_{East}$  and  $U_{North}$  are the current components in the original co-ordinate system pre-rotation. These components can be compared to the ADCP measurements.

Doppler shifts are a smooth quantity so sudden jumps in the data can easily be eliminated [21]. Curves are commonly fitted to the Doppler shifts to smoothen the data. Also, the NSP method represents the dispersion relation as single points. However, due to spectral leakage these points may not be that accurate hence it is valid to fit a curve to these Doppler shifts. These curves will also help with the current inversion.

To find a curve that fits the Doppler shifts we remove outliers from the rotated Doppler shifts. We add a velocity at  $z = 0$  to the ADCP data. Then we fit a 4<sup>th</sup> order polynomial to the ADCP data along with the point at  $z = 0$ . The corresponding Doppler shift curve is calculated using the polynomial fitting as the current profile  $U(z)$  in the Stewart and Joy integral from Equation (21). This is repeated for many different points at  $z = 0$ . For each point the RMSE is calculated between the NSP Doppler shifts and the Doppler shift curve for that point. The curve with the minimum value of RMSE is taken as the fitted curve to the Doppler shifts.

As an example, we can follow the process of fitting a curve to the raw  $U_{East}$  NSP points using the 18-23 data. Due to the large errors associated with the Doppler shifts for lower wavenumbers, we only consider Doppler shifts whose wavenumber is above  $k = 0.1$  rad/m. This improves estimates for lower wavenumbers as previously done for simulated data in Figure 8 and Figure 10. Using the remaining Doppler shifts a power law curve is fitted to the points. Points that are one standard deviation or more away from this curve are deemed as outliers shown in Figure 15 below.

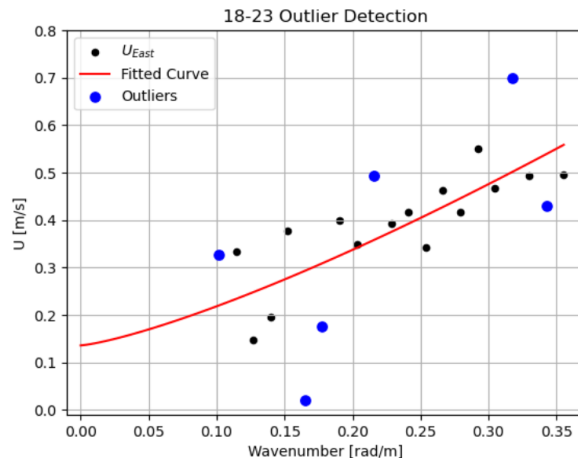


Figure 15: Shows the fitted curve to the filtered NSP points where the outliers have been detected based off their distance to the curve. Detected outliers are shown as blue points whereas non-outlier NSP points are shown as black points.

To aid the fitting process a velocity at the surface is added  $U_0$ . For this example we add a velocity of 0.8 m/s at  $z = 0$ . A polynomial is fitted to the ADCP data (blue points) along with the added artificial velocity (green point) resulting in Figure 16 on the left. This current profile can be used in the Stewart and Joy integral from Equation (21) to find the Doppler shift curve which has been shown in Figure 16 on the right.

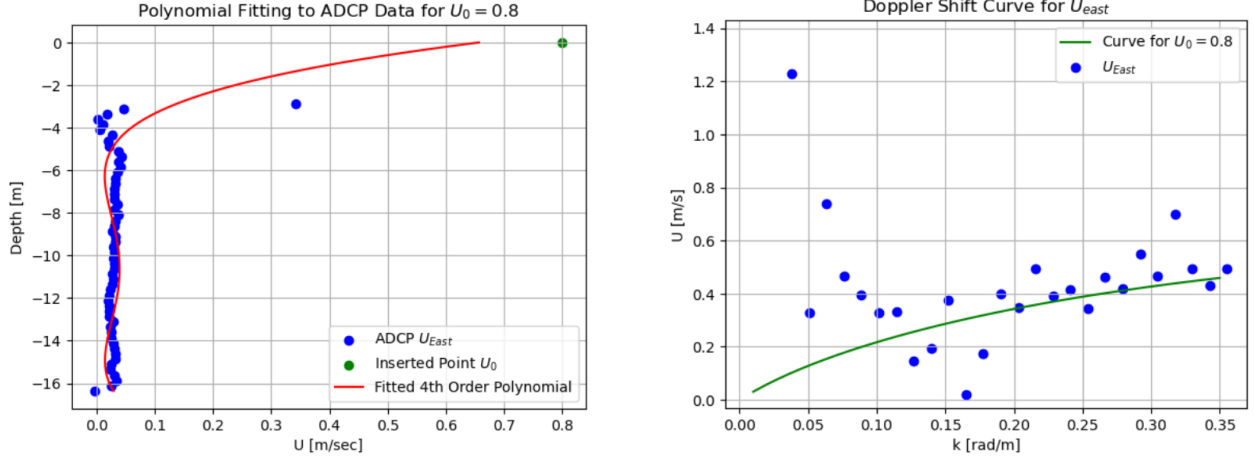


Figure 16: A polynomial is fitted to the ADCP data and  $U_0$  which results in the depth dependent current  $U(z)$  (left). This is used in the Stewart and Joy integral to give the estimate of the Doppler shift curve (right).

This process is repeated for many different values of  $U_0$  which range from the minimum value of the NSP Doppler shifts up to the maximum value of the NSP Doppler shifts. The curve with the minimum RMSE value is chosen to be the curve that fits the NSP Doppler shifts. The RMSE values for each component of each radar sequence are shown in Table 1 below:

Radar Sequence	RMSE ( $U_{\text{North}}$ )	RMSE ( $U_{\text{East}}$ )
18-21	0.033	0.061
19-04	0.068	0.057
19-11	0.043	0.096

Table 1: RMSE values between the Doppler shift curves and the NSP Doppler shift points for each of the radar sequences.

This method can be performed on each of the studied radar sequences. The NSP method is performed on each of the current components separately. The resulting Doppler shift points along

with the fitted Doppler shift curves are plotted in Figure 17.

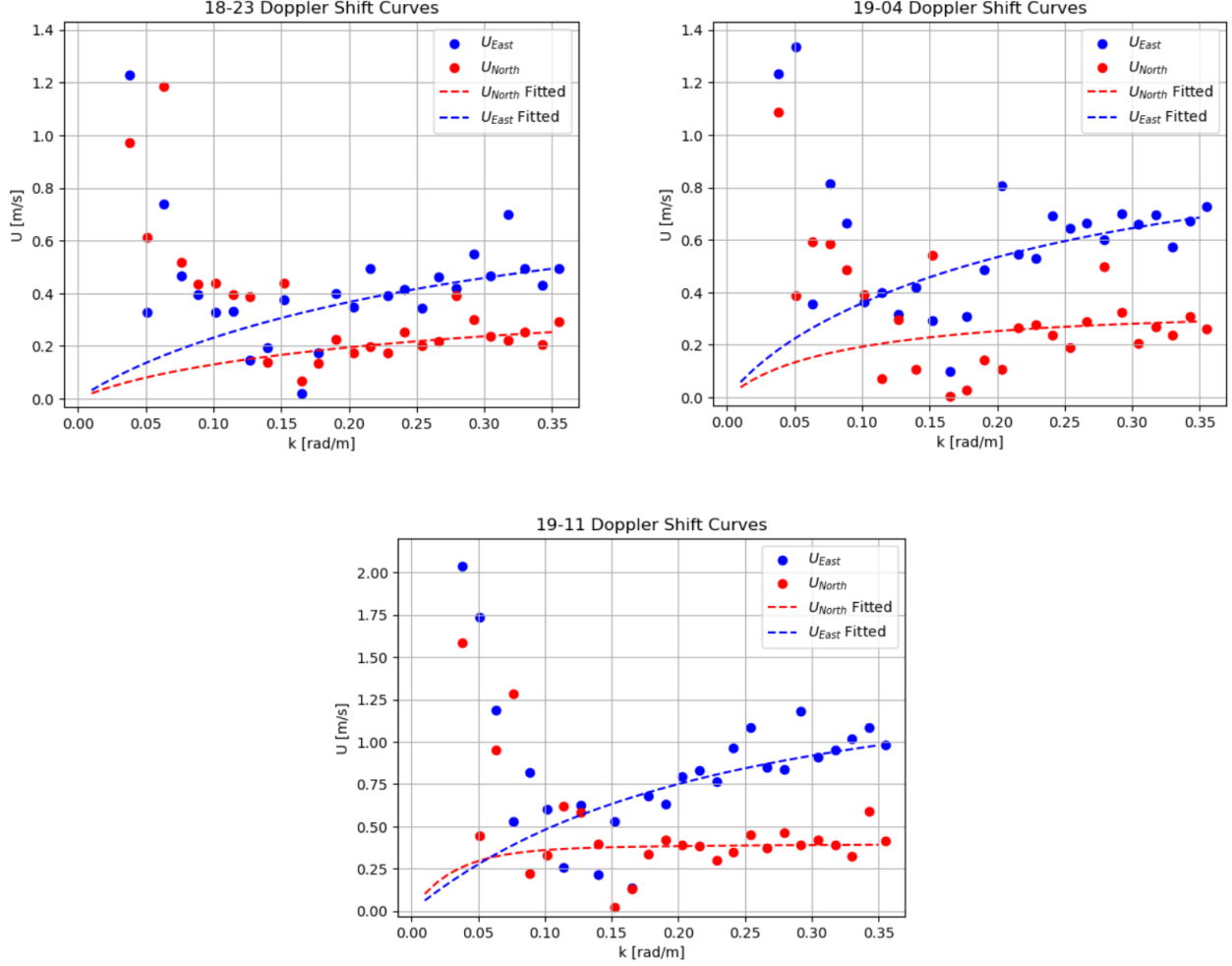


Figure 17: The fitted curves for both components of the Doppler shifts are plotted for the 18-23 (left) radar sequence, the 19-04 (right) radar sequence and the 19-11 (bottom) radar sequence. This method is applied to each component separately.

#### 4.4 Current Inversion

The fitted curves are used to represent the Doppler shifts for each component. The two inversion methods (EDM and PEDM) are used to find the depth-dependent current velocity  $U(z)$ . The PEDM is used as outlined in Section 3.2.2 with two main differences. Firstly, the monotonic assumption has been removed. This was originally added to the PEDM as it assumed the Doppler shifts are monotonic for almost all realistic curves. Doppler shifts are a smooth quantity due to the

Stewart and Joy integral from Equation (21). Inputting a current profile  $U(z)$  that has irregular jumps still results in smooth Doppler shifts,  $\tilde{c}(k)$ . However due to the fitting process we used, this assumption is not necessary as our Doppler shift curves are already a smooth quantity with no large jumps in the data. In Equations (29) and (30) it was assumed that the water had a large depth. However, in our case the water depth is much smaller at approximately  $h = 16$  m. Hence, the effective depth method is changed as the  $\tanh(kh)$  term can no longer be neglected. Thus, the effective depth of the current assuming a linear approximation is now:

$$Z_{eff}(k) = -(2k)^{-1} \tanh(kh), \quad (35)$$

where  $h = 16$  m is the depth of the water and  $k$  is the wavenumber. The remaining steps of the PEDM do not need to be changed which is outlined in Section 2.1.1 of Smeltzer *et al.* [35]. The performance of the PEDM is visible in Figures 18, 19 and 20 below. Both inversion methods are applied separately to the East and North components.

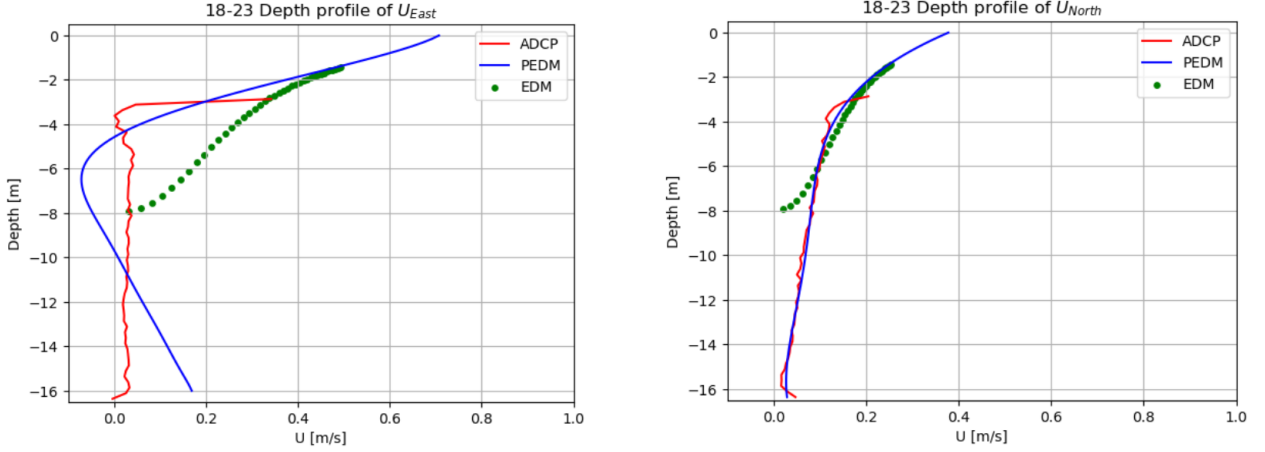


Figure 18: Current inversion methods are applied to the 18-23 radar sequence. Each method is plotted for the East component (left) and the North component (right).

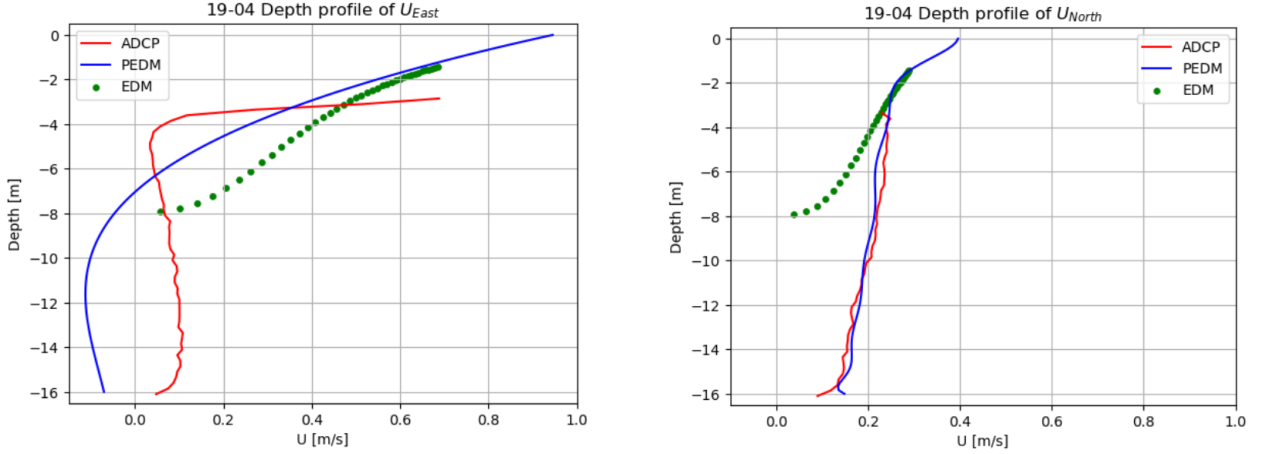


Figure 19: Current inversion methods are applied to the 19-04 radar sequence. Each method is plotted for the East component (left) and the North component (right).

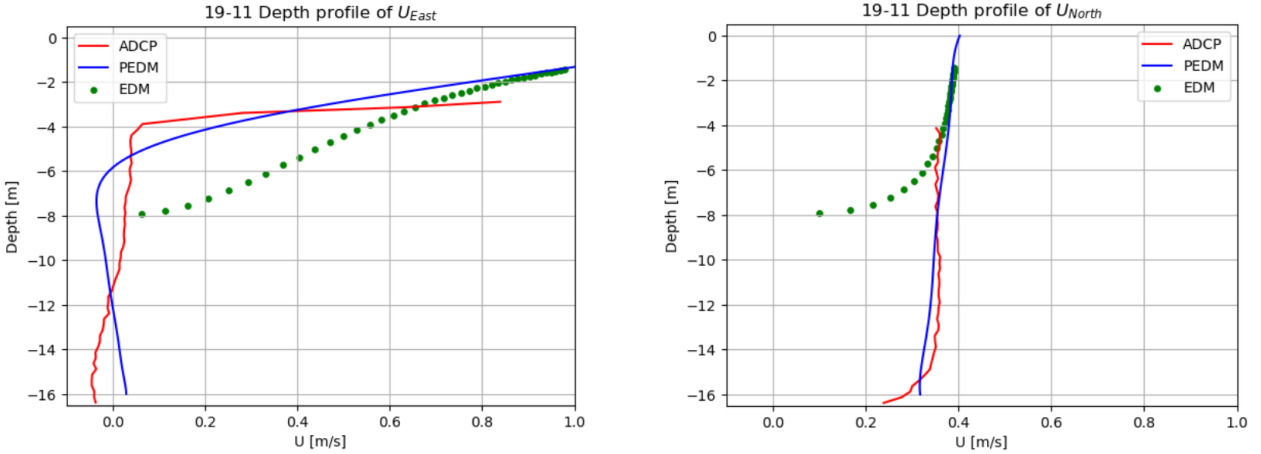


Figure 20: Current inversion methods are applied to the 19-11 radar sequence. Each method is plotted for the East component (left) and the North component (right).

#### 4.4.1 East Velocity Component

For each radar sequence the ADCP data suggests that there is a high amount of current shear in the  $U_{East}$  component. Quantifying shear for ADCP data is an ill-posed problem as it is difficult to differentiate the shear part and non-shear part of the current profile. Hence, for this study we will estimate the current shear visually.

For the East component neither the PEDM nor the EDM accurately find the current depth

profile. The PEDM performs best when the EDM is initially close to ADCP profile. For the EDM points to be close to the high shear initially we would require much larger Doppler shifts which were not seen in the data. This would have pointed to there being a very high current in the upper layers of the profile. However, we do not see these high Doppler shifts which is why the PEDM struggles to reconstruct the current profile.

The statistical discrepancy between the two methods is quantified in Table 2 below. We have calculated the average residuals between the ADCP data and the PEDM curve down to the greatest depth. We have also calculated the average residuals between the ADCP data and the EDM curve down to the smallest depth of the EDM at approximately  $z = 8$  m. The EDM clearly performs worse for this component than the PEDM. The best performance of the PEDM occurs for the 19-11 radar sequence. This is also the radar sequence which visually seems to have the least amount of shear despite having the highest velocities. This suggests that the PEDM performs best when the shear is the smallest.

Radar Sequence	EDM	PEDM
18-21	0.155	0.068
19-04	0.197	0.153
19-11	0.271	0.055

Table 2: Average residual values between the ADCP and each of the inversion methods for each radar sequence.

#### 4.4.2 North Velocity Component

The  $U_{North}$  component is reconstructed well by the PEDM for both radar sequences. For this component there is significantly less shear. The EDM points fit the upper part of the ADCP data well which means the PEDM performs much better than we saw in the  $U_{East}$  component case. This is evident in Figure 21 where we compare the PEDM and EDM at reconstructing the depth-dependent current for the effective depths. The EDM does not reconstruct the current lower in the water column very well. The PEDM is much better at finding the current for lower depths. The PEDM offers improvement over the EDM for these profiles which have less shear.

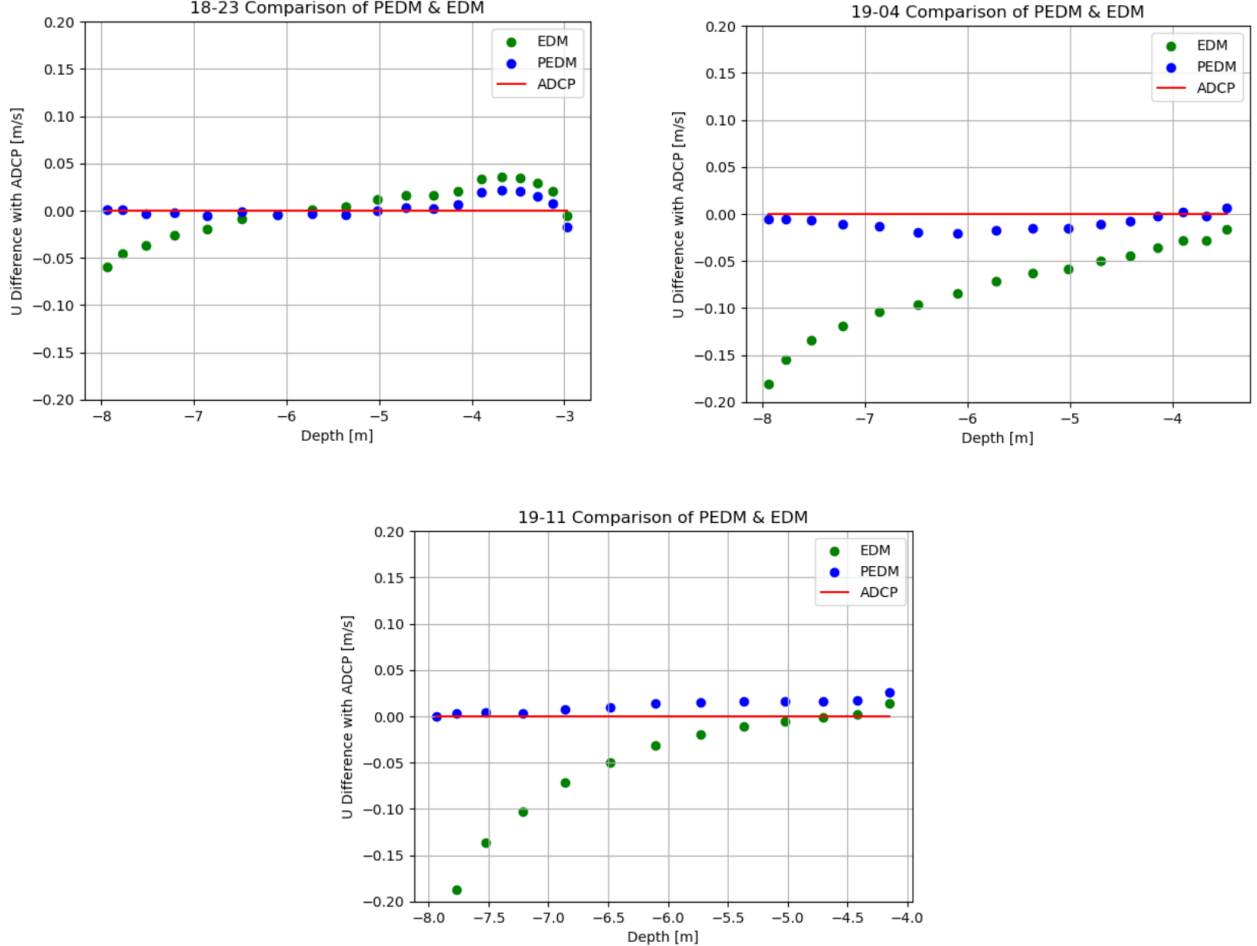


Figure 21: The PEDM and EDM are compared for  $U_{North}$  for each radar sequence. The difference with the ADCP measurements are plotted at depths where the EDM points are present.

## 4.5 Limitations

It is important to note some of the limitations and challenges associated with evaluating and interpreting our results. This work assumes that the radar images are an Eulerian measurement allowing for comparison with the ADCP which is also an Eulerian measurement. This assumption is based on findings that the Stokes drift is neither present in the radar image nor in the wave model [21]. However, the nature of radar measurements is somewhat ill-defined. Some previous studies suggest that radar images measure the Lagrangian current which includes Stokes drift [37].

The absolute accuracy of the PEDM is affected by the wave spectrum bandwidth [35]. The wave spectrum having a broader range of wavenumbers and directions is required for the reconstruction

of the depth profile. The need for a sufficient spectrum of waves will affect any method where currents are estimated from surface wave dispersion.

The current in the upper depths of the column is difficult to find due to the presence of waves. There are no accurate in situ methods for finding this current in the upper depths. Currents reconstructed by radar images are a good way of obtaining near surface currents. However, validation in the upper layers is difficult due to the lack of reliable truth measurements available in this region.

## 5 Conclusion

In this project we have discussed the factors that influence the accuracy of current retrieval using radar images. This study attempts to advance work in remote sensing for ocean wave currents.

We studied simulated waves. We applied the LS, NSP and PCS methods to find the wavenumber-dependent effective current. Errors due to spectral leakage were observed for lower wavenumbers. These errors were less prevalent in the NSP method than in the PCS method. The current reconstruction was also performed using the NSP and PCS methods where we saw the improved performance of the inversion methods using the NSP Doppler shifts. Thus, we concluded that the NSP method is more viable for finding accurate wavenumber-dependent Doppler shifts which agrees with results in other studies [25, 27]. The improvement of the PEDM over the EDM in finding the depth-dependent current was clear to see. This was as expected for simulated waves [35].

Waves from the Eastern Mediterranean Sea were used. The Doppler shifts of three radar image sequences were found where aliasing and spectral leakage were accounted for. These Doppler shift curves were used to invert the current profile. We performed the first test of the PEDM for real world ocean wave data. The improvement of the PEDM over the EDM was verified for these waves. The PEDM also provided an estimate of the current in shallower depths than the ADCP.

We also observed the effect shear has on the current inversion methods. This work has uncovered a limitation of the PEDM which is that the PEDM struggles to reconstruct currents with significant levels of shear. A natural extension of this work would be to quantify the level of shear required for the PEDM to break down. The PEDM could be improved to work for high shear situations by using in situ data at greater depths.

## Appendix

### A. Dispersion Relation on Uniform Current

Waves on top of a constant current can be represented using  $\vec{u} = U\hat{e}_x + \nabla\phi$ , where  $U$  is the constant current and  $\phi = \phi(x, z, t)$  is the velocity potential. The flow is assumed to be irrotational leading to the conservation of mass becoming Laplace's equation:

$$\nabla^2\phi = 0. \quad (36)$$

At the bottom of the ocean there is a no flux condition. This simplifies to a zero vertical velocity condition, for a flat bottom  $z = -h$  becoming:

$$\frac{\partial\phi}{\partial z} = 0 \quad , \quad z = -h. \quad (37)$$

### Kinematic Boundary Condition

Next, consider the conditions on the free surface. The free surface is given by  $z = \eta(x, t)$ . This holds for all time resulting in the kinematic boundary condition:

$$\frac{D}{Dt}(z - \eta(x, t)) = 0. \quad (38)$$

The definition of the material derivative can be used to give:

$$w = \frac{\partial\eta}{\partial t} + u\frac{\partial\eta}{\partial x} \quad , \quad z = \eta(x, t). \quad (39)$$

Now consider the definition of the constant current,  $u = U + \frac{\partial\phi}{\partial x}$  and  $w = \frac{\partial\phi}{\partial z}$ . Substituting this into Equation (39) while neglecting quadratic terms about still water gives:

$$\frac{\partial\phi}{\partial z} = \frac{\partial\eta}{\partial t} + U\frac{\partial\eta}{\partial x} \quad , \quad z = 0. \quad (40)$$

## Dynamic Boundary Condition

The dynamic boundary condition uses  $p = p_a$  in the Bernoulli equation on  $z = \eta(x, t)$ . The velocity potential is unique up to an additive constant and so  $\phi$  can be re-scaled to give the unsteady Bernoulli equation on constant current which is:

$$\frac{\partial \phi}{\partial t} + g\eta + \frac{1}{2} \left( \left( U + \frac{\partial \phi}{\partial x} \right)^2 + \left( \frac{\partial \phi}{\partial z} \right)^2 \right) = 0 \quad , \quad z = \eta(x, t). \quad (41)$$

Neglecting quadratic terms again gives the dynamic boundary condition:

$$\frac{\partial \phi}{\partial t} + g\eta + U \frac{\partial \phi}{\partial x} = 0 \quad , \quad z = 0. \quad (42)$$

## Harmonic Solutions

Now that we have the governing system for linear water waves in a constant current from Equations (36), (37), (40) and (42), we seek harmonic solutions:

$$\eta(x, t) = A \cos(kx - \omega t - \beta), \quad (43)$$

$$\phi(x, z, t) = f(z) \sin(kx - \omega t - \beta). \quad (44)$$

where  $\beta$  is a phase shift to a specified initial condition. The velocity potential in Laplace's equation yields:

$$\frac{d^2 f}{dz^2} - k^2 f = 0. \quad (45)$$

This has solution  $f(z) = B \cosh(kz) + C \sinh(kz)$  for constants  $B$  and  $C$ . Applying the boundary condition from Equation (37) gives  $C$  in terms of  $B$  which can be put back into the solution of Equation (45) resulting in:

$$f(z) = B \frac{\cosh(k(z + h))}{\cosh(kh)}. \quad (46)$$

Thus,

$$\phi(x, z) = B \frac{\cosh(k(z + h))}{\cosh(kh)} \sin(kx - \omega t - \beta). \quad (47)$$

Put this new velocity potential along with  $\eta(x, t)$  into the kinematic boundary condition in Equation (40). This results in:

$$\left( Bk \frac{\sinh(kh)}{\cosh(kh)} - \omega A + U k A \right) \sin(kx - \omega t - \beta) = 0. \quad (48)$$

Similarly, putting the velocity potential and  $\eta(x, t)$  into the dynamic boundary condition in Equation (42) yields:

$$(-\omega B + gA + UkB) \cos(kx - \omega t - \beta) = 0. \quad (49)$$

Equations (48) and (49) can be represented by a matrix system.

$$\begin{pmatrix} -\omega + U k & k \tanh(kh) \\ g & -\omega + U k \end{pmatrix} \begin{pmatrix} A \\ B \end{pmatrix} = \begin{pmatrix} 0 \\ 0 \end{pmatrix}. \quad (50)$$

Taking the determinant of the resulting matrix to be 0 yields:

$$(\omega - U k)^2 = gk \tanh(kh). \quad (51)$$

The positive root of this equation is taken as we are interested travelling in the direction of the wave energy. Resulting in the dispersion relation for ocean waves on a uniform current in 1D:

$$\omega = \sqrt{gk \tanh(kh)} + U k. \quad (52)$$

## B. Triplet Extraction

The dispersion relation triplets will be found using the following method as outlined in Shen *et al.* [13]. The three-dimensional array of sea surface images is denoted as  $I(x, y, t)$  as before. The sub-image is usually chosen to be square ( $N \times N$ ) so that the resolution in wavenumber in both directions will be the same [30]. Thus,  $I(x, y, t)$  will have a size of  $N \times N \times M$  pixels, with  $M$  corresponding to the duration of the time series. The dispersion triplets can be found using the following method:

1. *3D FFT*: The sub-image sequence can be multiplied by a smooth tapering function to mitigate

the Gibbs phenomenon in both spatial and temporal domains [38]. Zero padding is then used to increase the original data size ( $N \times N \times M$ ) to a larger number of pixels in each domain which can result in a smoother image at a cost of computing time. A 3D FFT is applied to the larger image spectrum resulting in the power spectrum  $I(k_x, k_y, \omega)$ .

2. *Extraction of Dispersion Shell:* Next, the dispersion shell is extracted using the peaks of the power spectrum through the following steps:

(A) *High Pass Filter:* The non-stationary and non-homogenous trends in the sub-image sequence are removed using a high pass filter on  $I(k_x, k_y, \omega)$  which gives:

$$I_1(k_x, k_y, \omega) = \begin{cases} 0, & \text{if } \omega < \omega_{\text{cut}} \\ I(k_x, k_y, \omega), & \text{if } \omega \geq \omega_{\text{cut}} \end{cases} \quad (53)$$

where the cutoff frequency is usually taken as  $\omega_{\text{cut}} = 0.03 \times 2\pi$  radians/s [39].

(B) *Energy Threshold:* For every pair  $(k_{xi}, k_{yj})$  there is a singular column vector of energy  $I_1(k_{xi}, k_{yj}, \omega)$  with  $i, j = 1, 2, \dots, N$ . If the maximum energy  $E_{\max-ij} = \max\{I_1(k_{xi}, k_{yj}, \omega)\}$  in this column is not larger than  $\bar{P}$  then this column is disregarded as having a low energy. The threshold is defined by the maximum energy in the entire spectrum,  $E_{\max}$ , using  $\bar{P} = E_{\max}/2000$ . This eliminates possible interference from low-energy noise spikes:

$$I_2(k_{xi}, k_{yj}, \omega) = \begin{cases} 0, & \text{if } E_{\max-ij} < \bar{P} \\ I_1(k_{xi}, k_{yj}, \omega), & \text{if } E_{\max-ij} \geq \bar{P} \end{cases} \quad (54)$$

(C) *Peak Identification:* Only one frequency point  $\omega_q$  is associated with each wave-vector pair. To find this we examine the frequencies observed at each wave-vector pair. Prominent peaks are defined as no other peak reaches one-third of the maximum peak. If there is only one prominent peak then the frequency of this peak  $\omega_q$  is used. If there are no prominent peaks then  $\omega_q$  is 0.

All of the extracted non-zero  $\omega_q$  can be grouped with their corresponding wavenumber which gives  $(k_{xi}, k_{yj}, \omega_q)$ . These are the dispersion relation triplets similarly shown in Figure 1.

### C. PCS Fitting on Field Data

For example, the PCS method is applied to the 19-04 radar sequence. The triplets are anti-aliased leading to more triplets at higher wavenumbers. Following the steps in Section 3.1.3 the fitting process is performed. However, looking at the triplets being fitted in Figure 22 (left) there is a clear poor fitting of the sinusoid. This same poor fitting occurs for all radii of the dispersion shell. Thus, the PCS method gets inaccurate velocities. The PCS also only finds velocities for a limited number of wavenumbers shown in Figure 22 (right) which is caused by the PCS requiring at least 10 points to be fitted for each wavenumber.

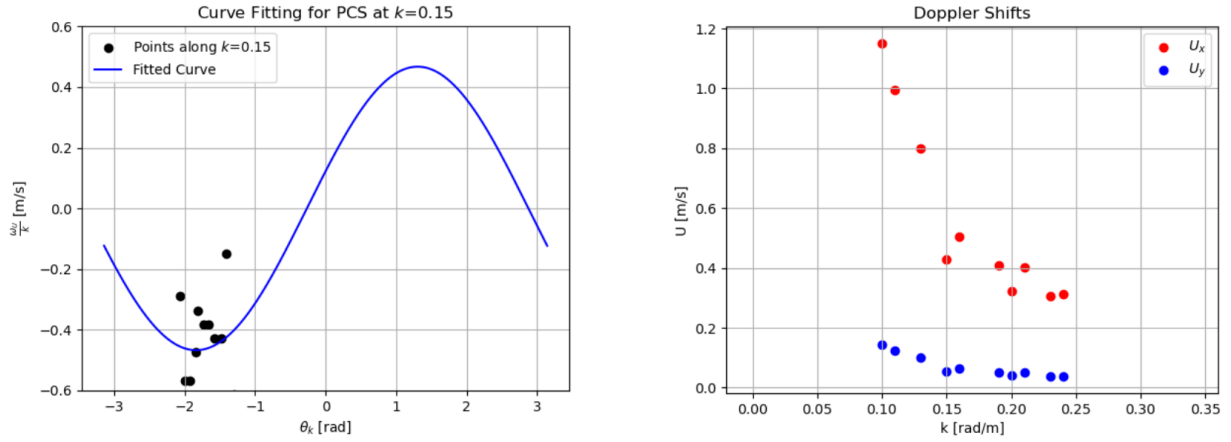


Figure 22: The fitting of the current shell at a particular radius  $k = 0.15$  (left). The PCS is performed for many different wavenumbers (right).

These tendencies were observed in the fitting of the other two radar sequences as well. This resulted in inaccurate estimations of the Doppler shifts.

## References

- [1] N. Pinardi et al. "From weather to ocean predictions: an historical viewpoint". In: *Journal of Marine Research* 75 (2017), pp. 103–159.
- [2] T. C. Royer et al. "Ocean Circulation Influencing the "Exxon Valdez" Oil Spill". In: *Oceanography* 3.2 (1990), pp. 3–10.
- [3] Y.-C. Chang et al. "Ship routing utilizing strong ocean currents". In: *The Journal of Navigation* 66.6 (2013), pp. 825–835.
- [4] N. Hidayati et al. "Ocean currents energy for electricity generation and its potential in East Java water, Indonesia". In: *Journal of Environmental Engineering and Sustainable Technology* 3.2 (2016), pp. 104–111.
- [5] N. Fofonoff and F. Webster. "A discussion on ocean currents and their dynamics-current measurements in the Western Atlantic". In: *Philosophical Transactions of the Royal Society of London. Series A, Mathematical and Physical Sciences* 270.1206 (1971), pp. 423–436.
- [6] K. Taira et al. "Current measurements with surface and subsurface drifters". In: *Journal of the Oceanographical Society of Japan* 34 (1978), pp. 73–77.
- [7] R. H. Stewart. "Introduction to physical oceanography". In: OAKTrust, 2008. Chap. 10: Geostrophic Currents.
- [8] T. Chereskin and A. Harding. "Modeling the performance of an acoustic Doppler current profiler". In: *Journal of Atmospheric and Oceanic Technology* 10.1 (1993), pp. 41–63.
- [9] R. Davis, R DeSzeke, and P Niiler. "Variability in the upper ocean during MILE. Part II: Modeling the mixed layer response". In: *Deep Sea Research Part A. Oceanographic Research Papers* 28.12 (1981), pp. 1453–1475.
- [10] M. G. Mattie and D. L. Harris. "The use of imaging radar in studying ocean waves". In: *16th Coastal Engineering Conference*. (1978), pp. 174–189.

- [11] P. Naaijen and E. Blondel-Couprie. “Reconstruction and prediction of short-crested seas based on the application of a 3D-FFT on synthetic waves: Part 1—reconstruction”. In: *International Conference on Offshore Mechanics and Arctic Engineering*. Vol. 44922. American Society of Mechanical Engineers. (2012), pp. 43–53.
- [12] B. K. Smeltzer and S. Å. Elling. “Current Mapping from the Wave spectrum”. In: *iOcean Remote Sensing Technologies: High frequency, Marine and GNSS-Based Radar*. Ed. by W. Huang and E. G. Stevenage: SciTech Publish, (2004). Chap. 15, pp. 357–378.
- [13] C. Shen et al. “An algorithm for surface current retrieval from X-band marine radar images”. In: *Remote Sensing* 7.6 (2015), pp. 7753–7767.
- [14] R. H. Stewart and J. W. Joy. “HF radio measurements of surface currents”. In: *Deep Sea Research and Oceanographic Abstracts*. Vol. 21. Elsevier. (1974), pp. 1039–1049.
- [15] C.-S. Yih. “Surface waves in flowing water”. In: *Journal of Fluid Mechanics* 51.2 (1972), pp. 209–220.
- [16] D. J. Acheson. *Elementary Fluid Dynamics*. Clarendon Press, (1992), pp. 65–74.
- [17] R. G. Dean. “Stream function representation of nonlinear ocean waves”. In: *Journal of Geophysical Research* 70.18 (1965), pp. 4561–4572.
- [18] R. A. Skop. “Approximate dispersion relation for wave-current interactions”. In: *Journal of Waterway, Port, Coastal, and Ocean Engineering* 113.2 (1987), pp. 187–195.
- [19] J. T. Kirby and T.-M. Chen. “Surface waves on vertically sheared flows: approximate dispersion relations”. In: *Journal of Geophysical Research: Oceans* 94.C1 (1989), pp. 1013–1027.
- [20] H. Mitsuyasu et al. “Observations of the directional spectrum of ocean Waves Using a cloverleaf buoy”. In: *Journal of Physical Oceanography* 5.4 (1975), pp. 750–760.
- [21] B. Keeler Smeltzer, S. Støle-Hentschel, and Y. Toledo. “On the measurement of the dispersion relation by a radar and the implication on the current retrieval”. In: *arXiv e-prints* (2023).
- [22] I. R. Young, W Rosenthal, and F Ziemer. “A three-dimensional analysis of marine radar images for the determination of ocean wave directionality and surface currents”. In: *Journal of Geophysical Research: Oceans* 90.C1 (1985), pp. 1049–1059.

- [23] R. Gangeskar. “Ocean current estimated from X-band radar sea surface, images”. In: *IEEE Transactions on Geoscience and Remote Sensing* 40.4 (2002), pp. 783–792.
- [24] C. M. Senet, J. Seemann, and F. Ziemer. “The near-surface current velocity determined from image sequences of the sea surface”. In: *IEEE Transactions on Geoscience and Remote Sensing* 39.3 (2001), pp. 492–505.
- [25] F. Serafino, C. Lugni, and F. Soldovieri. “A novel strategy for the surface current determination from marine X-band radar data”. In: *IEEE Geoscience and Remote Sensing Letters* 7.2 (2009), pp. 231–235.
- [26] C. Shen, W. Huang, and E. W. Gill. “An alternative method for surface current extraction from X-band marine radar images”. In: *2014 IEEE Geoscience and Remote Sensing Symposium*. IEEE. (2014), pp. 4370–4373.
- [27] W. Huang and E. Gill. “Surface current measurement under low sea state using dual polarized X-band nautical radar”. In: *IEEE Journal of Selected Topics in Applied Earth Observations and Remote Sensing* 5.6 (2012), pp. 1868–1873.
- [28] W. Huang, E. Gill, and J. An. “Iterative least-squares-based wave measurement using X-band nautical radar”. In: *IET Radar, Sonar & Navigation* 8.8 (2014), pp. 853–863.
- [29] W. Huang et al. “Surface current measurements using X-band marine radar with vertical polarization”. In: *IEEE Transactions on Geoscience and Remote Sensing* 54.5 (2016), pp. 2988–2997.
- [30] S. Weichert, B. K. Smeltzer, and S. Å. Ellingsen. “Biases from spectral leakage in remote sensing of near-surface currents”. In: *IEEE Transactions on Geoscience and Remote Sensing* (2023), pp. 1–16.
- [31] F. E. Grubbs. “Procedures for detecting outlying observations in samples”. In: *Technometrics* 11.1 (1969), pp. 1–21.
- [32] J. Campana, E. J. Terrill, and T. De Paolo. “The development of an inversion technique to extract vertical current profiles from X-band radar observations”. In: *Journal of Atmospheric and Oceanic Technology* 33.9 (2016), pp. 2015–2028.

- [33] B. Lund et al. “A new technique for the retrieval of near-surface vertical current shear from marine X-band radar images”. In: *Journal of Geophysical Research: Oceans* 120.12 (2015), pp. 8466–8486.
- [34] D. M. Fernandez, J. F. Vesecky, and C. C. Teague. “Measurements of upper ocean surface current shear with high-frequency radar”. In: *Journal of Geophysical Research: Oceans* 101.C12 (1996), pp. 28615–28625.
- [35] B. K. Smeltzer et al. “An improved method for determining near-surface currents from wave dispersion measurements”. In: *Journal of Geophysical Research: Oceans* 124.12 (2019), pp. 8832–8851.
- [36] S. Støle-Hentschel et al. “Extreme wave statistics of counter-propagating, irregular, long-crested sea states”. In: *Physics of Fluids* 30.6 (2018), p. 067102.
- [37] N. Pizzo et al. “The role of Lagrangian drift in the geometry, kinematics and dynamics of surface waves”. In: *Journal of Fluid Mechanics* 954 (2023), R4.
- [38] J. W. Tukey. “An introduction to the calculation of numerical spectrum analysis”. In: *Spectra Analysis of Time Series* (1967), pp. 25–46.
- [39] J. N. Borge and C. G. Soares. “Analysis of directional wave fields using X-band navigation radar”. In: *Coastal Engineering* 40.4 (2000), pp. 375–391.